CrossMark

ORIGINAL PAPER

Coastal uplift west of Algiers (Algeria): pre- and post-Messinian sequences of marine terraces and rasas and their associated drainage pattern

Christine Authemayou[1] · Kevin Pedoja[2,3,4] · Aicha Heddar[5] · Stéphane Molliex[1] ·
Azzedine Boudiaf[5] · Bassam Ghaleb[6] · Brigitte Van Vliet Lanoe[1] ·
Bernard Delcaillau[2,3,4] · Hamou Djellit[5] · Karim Yelles[5] · Maelle Nexer[2,3,4]

Abstract The North Africa passive margin is affected by the ongoing convergence between the African and Eurasian plates. This convergence is responsible for coastal uplift, folding, and reverse faulting on new and reactivated faults on the margin. The active deformation is diffuse and thus rather difficult to locate precisely. We aim to determine how a coastal landscape evolve in this geodynamic setting and gain insights into active tectonics. More particularly, we evidence and quantify coastal uplift pattern of the Chenoua, Sahel, and Algiers reliefs (Algeria), using sequences of marine terraces and rasas and computing several morphometric indices from the drainage pattern. Upper and Middle Pleistocene uplift rates are obtained by fossil shoreline mapping and preliminary U/Th dating of associated coastal deposits. Extrapolation of these rates combined to analyses of sea-level referential data and spatial relationships between marine terraces/rasas and other geological markers lead us to tentatively propose an age for the highest coastal indicators (purported the oldest). Values of morphometric indices showing correlations with uplift rate allow us to analyze uplift variation on area devoid of coastal sequence. Geological and geomorphological data suggest that coastal uplift probably occurred since the Middle Miocene. It resulted in the emergence of the Algiers massif, followed by the Sahel ridge massif. The Sahel ridge has asymmetrically grown by folding from west to east and was affected by temporal variation of uplift. Compared to previous study, the location of the Sahel fold axis has been shifted offshore, near the coast. The Chenoua fault vertical motion does not offset significantly the coastal sequence. Mean apparent uplift rates and corrected uplift rates since 120 ka are globally steady all along the coast with a mean value of 0.055 ± 0.015 mm/year (apparent) and of 0.005 ± 0.045 mm/year (corrected for eustasy). Mean apparent coastal uplift rates between 120 and 400 ka increase eastward from 0.045 ± 0.025 to 0.19 ± 0.12 mm/year (without correction for eustasy) or from 0.06 ± 0.06 to 0.2 ± 0.15 mm/year (with correction for eustasy). In addition, the combination of structural and geomorphic data suggests a low uplift rate for the southern part of the Algiers massif.

✉ Christine Authemayou
christine.authemayou@univ-brest.fr

[1] Laboratoire Domaines océaniques, UMR 6538- IUEM, Université de Brest, CNRS, Brest, Plouzané, France

[2] Normandie Université, Caen, France

[3] UCBN, M2C, 14000 Caen, France

[4] UMR 6143 M2C, CNRS, 14000 Caen, France

[5] CRAAG : Centre de Recherche en Astronomie, Astrophysique et géophysique, Route de l'observatoire, BP63, Bouzareah, Algiers, Algeria

[6] GEOTOP-UQAM-McGILL, Université du Québec, Montréal, Canada

Introduction

Tectonic inversion of passive margins by compression generally implies diffuse deformation with tilting, folding, or motions on both new reverse structures and inherited faults formed during the rifting phase (Sten et al. 1989; Cloethingh et al. 1989; Wolin et al. 2012). Determining the location of active structures is consequently difficult but essential because strong earthquakes may occur in these areas often densely populated. The North African margin is

🌀 Springer

one of the best examples of inverted passive margin (Serpelloni et al. 2007) presently affected by active compression (Leprêtre et al. 2013 and references therein) and major seismic events (Ms: 7.3 El Asnam event in 10/10/1980,Mw 6.8 Boumerdes event in 05/21/2003; Harbi et al. 2004; 2007). Active deformation is evidenced by emerged sequences of fossil shorelines described from southwestern Morocco to eastern Libya along a 4 500-km stretch of coast (e.g., Pedoja et al. 2011, 2013, 2014 and reference therein). The coast located to the west of Algiers city (Algeria) exhibits particularly well-preserved coastal sequences and presents active structures that need to be better characterized since this densely populated region has been affected by strong earthquakes (Harbi et al. 2004, 2007; Heddar et al. 2013) (Fig. 1a).

In order to determine the segmentation of active faults and fold systems as well as their deformation rates, we propose a cross-analysis of coastal sequences (marine terraces and rasas) with a quantitative geomorphic study of the regional drainage pattern. Emerged coastal land presents some advantages to infer tectonic motions because the staircase morphology of the sequence, its associated drainage pattern, and the lithology are rather simple; moreover, the climate regime is homogeneous. Mapping and dating the fossil shorelines aim to constrain the local chronostratigraphy and to quantify coastal uplift rates for different time periods and at different location along the coast. Then, correlations between morphometric parameters and uplift rates (e.g., Nexer et al. 2015) on catchments located along the same stretch of the Algerian coast, as well as on the hinterlands, allow to complete information on uplift gradient especially where no sequence of fossil shorelines are present. Besides the tectonic issue, this approach also allows to investigate the geomorphic evolution of the studied zone.
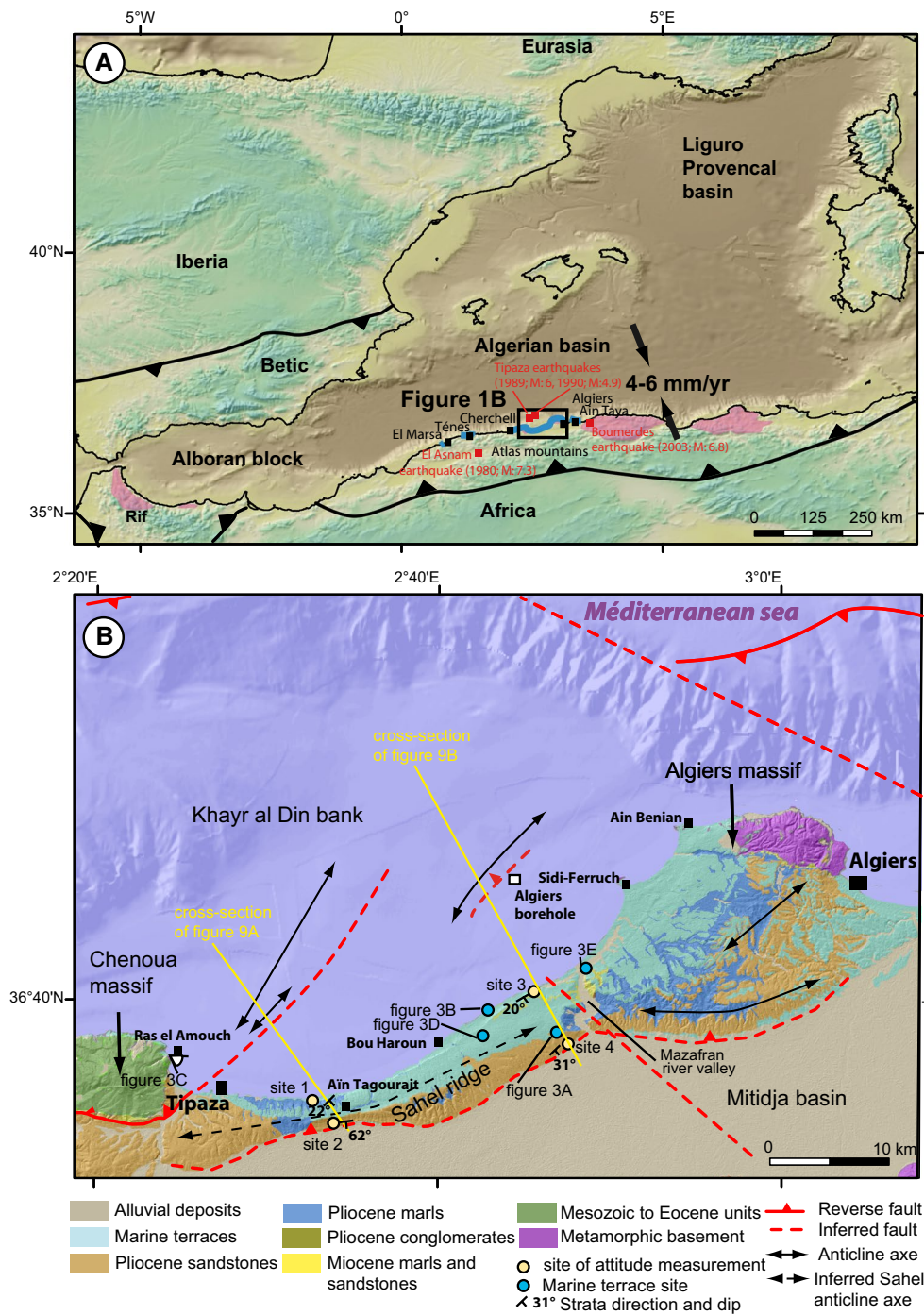
Settings

Geodynamics

We studied a 70-km-long coastal stretch, located west of Algiers, along the Mediterranean shores (Fig. 1a). This coastal stretch belongs to the passive margin of the Algerian back-arc basin which opened during the Oligocene because of the southward rollback of the Tethyan oceanic slab subducting under the southern boundary of the Kabylian blocks (Carminati et al. 1998; Frizon De Lamotte et al. 2000; Jolivet and Faccenna 2000; Duggen et al. 2004; Mauffret et al. 2004; Schettino and Turco 2006). These blocks, separated by NW–SE strike-slip faults, originated from Eurasia and were pulled southward by slab rollback until they collided with the African plate

during the Lower Miocene (Raymond 1976; Bouillin 1992; Bracène and Frizon de Lamotte 2002; Schettino and Turco 2006). The spreading of the Algerian basin ended at ~20–16 Ma, during the collision between the Kabylian blocks and the African plate, and synchronous with a slab break-off event (Carminati et al. 1998; Maury et al. 2000; Rosenbaum and Lister 2004; Schettino and Turco 2006). During Middle Miocene (Langhian–Serravalian), the Tellian nappes associated with the Kabylian blocks collision were sealed by marine deposits affected by NNW-SSE extension (Aïté and Gélard 1997). This extensional phase was recorded in the Mitidja region (Boudiaf 1996). This period of quiescence ended during Late Miocene times when the Eurasia–Africa convergence reactivated the margin by compression (Thomas 1976; Domzig et al. 2006; Yelles et al. 2009; Strzerzynski et al. 2010).

The present convergence rate between Eurasia and Africa is ~4–6 mm/year (Fig. 1a) (Nocquet and Calais 2004). Its strike changed from N–S to NW–SE, ~3 Ma ago (DeMets et al. 1990; Rosenbaum et al. 2002; Calais et al. 2003; Stich et al. 2006; Serpelloni et al. 2007). This shortening is accommodated by faulted and folded structures located onshore and offshore (Thomas 1976; Philip and Meghraoui 1983; Ambraseys and Vogt 1988; Domzig et al. 2006; Yelles et al. 2006; Strzerzynski et al. 2010; Medaouri et al. 2012). The most famous fault in Algeria is the NE–SW sinistral reverse Oued Fodda fault, commonly known as El Asnam fault, which generated the strongest earthquake so far in the western Mediterranean, on October 10, 1980 (Ms: 7.3) (King and Vita Finzi 1981; Meghraoui et al. 1988) (Fig. 1a). Other strong earthquakes ($M > 7$) affected northern Algeria in recent times (e.g., Harbi et al. 2004, 2007), including the Mw 6.8 Boumerdes event (05/21/2003) which probably induced 20–30 cm of coseismic coastal uplift (Meghraoui et al. 2004; Maouche et al. 2011) and reactivated offshore structures (Déverchère et al. 2005, 2010) (Fig. 1a).

Geology

We studied the structures ("folds" and faults) located between the Chenoua and Algiers massifs (Fig. 1b) which are relics of Kabylian blocks spread along the coast during Miocene times (Durand-Delga 1969). The Algiers massif consists of a crystalline metamorphic basement, whereas the Chenoua massif exhibits the sedimentary cover of the Kabylian blocks, the latter sediments being Mesozoic to early Eocene marine deposits (Peucat et al. 1996). The Algiers massif is bounded to the north (i.e., offshore) by a reverse south-dipping active fault located at the foot of the margin (Yelles et al. 2009). To the south (i.e., onshore), the massif is bounded by two anticlines associated with

Fig. 1 Settings of the Algerian margin. **a** Geodynamics of the western Mediterranean. *Blue line* corresponds to the marine terrace and rasa mapping area. Pink areas correspond to Kabylian blocks. *Black arrows* with value in mm/year indicate the convergence vector between Africa and Europe (Nocquet and Calais 2004). *Black line* with triangles indicates the thrust front of this convergence. **b** Geology of the Sahel ridge area, west of Algiers (*redrawn* from Strzerzynski et al. 2010; Maouche et al. 2011)

a potential southern blind south-verging reverse fault (Fig. 1b) (Harbi et al. 2004; Domzig et al. 2006). The Chenoua massif is bounded to the south by a north-dipping onshore reverse fault bent northeastward in the offshore domain and reactivated in 1989 (Meghraoui 1991). East of

this structure, two offshore, NE–SW-trending, en-echelon anticlines are most probably associated with a reverse fault affecting Pliocene sedimentary units (Zanclean–Piacenzian) (Domzig et al. 2006; Yelles et al. 2009; Strzerzynski et al. 2010).

The 60-km-long WSW-ENE Sahel ridge extends between the two massifs (Fig. 1b) and corresponds to the northern boundary of the Middle Miocene to Quaternary intra-continental Mitidja basin (Glangeaud et al. 1952; Aymé et al. 1954). Different interpretations of this structure have been proposed. For Glangeaud (1932), Meghraoui (1991), and Maouche et al. (2011), it corresponds to an anticline associated with the propagation of a south-verging fault. For Aymé et al. (1954) and Yassini (1975), the ridge consists in a southward dipping monocline affecting the Mio-Pliocene sedimentary series (marls and sandstones Tortonian-Zanclean and Piacenzian in age). The deformation would be associated with the north-dipping blind thrust observed on the southern flank of the Sahel ridge (Meghraoui 1991; Maouche et al. 2011; Heddar et al. 2013). Modeling of recent gravity data highlighted a deep, steep north-dipping tectonic contact-oriented NE–SW between the Sahel ridge and the Mitidja basin (Hamaï 2011). Between the NE–SW Sahel ridge and the southern fold of the Algiers massif, the Mazafran River forms an across-strike valley (Fig. 1b).

Exposed on the eastern flank of Mazafran river valley, the boundary between the Miocene and Pliocene series consists in an erosional discordance on which continental conglomerates lay down (Aymé et al. 1954; Yassini 1975). The Pliocene deposits around the Mitidja basin have been interpreted as the infilling of canyons resulting from the sea-level rise after the Messinian salinity crisis (5.9–5.33 Ma) (Rubino et al. 2007). In the Algiers massif, the Pliocene units (maximum elevation of ~300 m) were considered by Rubino et al. (2007) to be a Gilbert-type delta showing a transition from marine to continental environments, evidenced by bottom set, foreset, and topset features (Gilbert 1899; Clauzon and Rubino 1992). The Pliocene deposits of the eastern flank of Mazafran river valley are considered as located upstream to the Algiers massif Pliocene outcrops but belonging also to the Gilbert-type delta deposits (Rubino et al. 2007). The Piacenzian age (3.6–2.6 Ma) of the marls (Yassini 1975) chronologically constraints the filling of the Algiers canyon. The transition between marine and continental deposits within the Pliocene units is related to the highest Pliocene-Quaternary highstand (the so-called Mid-Pliocene warm period highstand (3.3–2.9 Ma, e.g., Rovere et al. 2014)) in Mediterranean regions (Clauzon et al. 1996; Mocochain et al. 2006; Rubino et al. 2007). The Pliocene Gilbert-delta surface was probably abandoned following to a sea-level fall due to the Late Cenozoic intensification of glacio-eustatic cycles, synchronic with the development of the large ice sheets in the Northern Hemisphere (Clauzon et al. 1996; Rubino and Clauzon 2008), that started at ~3.3 Ma (Kleiven et al. 2002) and widespread at 2.6 Ma (Gibbard et al. 2010).

Previous studies on marine terraces west of Algiers

The northern flank of the Sahel ridge exhibits a staircase morphology (e.g., De Lamothe 1911). Up to the twenty-first century, only the associated sediments and malacological contents of the terraces and rasas were described (De Lamothe 1911; Glangeaud 1932; Aymé 1952; Saoudi 1988; 1989); the general distribution of the fossil shorelines west of Algiers being mapped recently (Maouche et al. 2011; this study). The initial chronomorphostratigraphy along the Sahel shores included three main stages of terrace formation following to the "old Mediterranean" Pleistocene terminology: the Sicilian-Calabrian (~120 ka–2.6 Ma), Tyrrhenian (~10–120 ka), and Versilian (<~10 ka) stages (De Lamothe 1911; Glangeaud 1932; Aymé 1952; Saoudi 1989). *Strombus bubonius* fossils found in the deposits of a low terrace (elevation <10 m, ~6 m as suggested in Saoudi 1989) were dated using the U/Th method at two sites between Tipaza and Aïn Tagourait and yielded two ages of 140 ± 10 ka and 125 ± 10 ka (Stearns and Thurber 1965) (Fig. 1b). This dating led the authors to correlate the lowest terrace to the last interglacial maximum (MIS 5e ~120 ka). This interpretation allows to calculate low uplift rates (~0.1 mm/year) for this coastal stretch, similar to those estimated in several places along the North Africa margin (e.g., Meghraoui et al. 1996; Morel and Meghraoui 1996; Pedoja et al. 2013, 2014).

Recently, Maouche et al. (2011) through ^{14}C dating and a postulate on the elevation of Stearns and Thurber's (1965) sampling reassessed the coastal uplift rate to be ~0.84–1.2 mm/year since 140 ka and ~2.5 mm/year for the last 31 ka. These authors interpreted their results as the incremental folding uplift since the Late Pleistocene and produced a model of fault-related fold growth in order to estimate the coseismic surface deformation and the possible occurrence of large earthquakes with Mw ≥ 7. Members of our team (Pedoja et al. 2013) raised major issues on the methods and results of this paper (Pedoja et al. 2013). The new data brought in the present work will help deciphering the timing and paleogeographical evolution of this densely populated coastal stretch.

Methods

Coastal sequences as indicators of tectonic activity

Staircase coastal sequences are widespread geomorphic markers (Lajoie, 1986; Murray-Wallace and Woodroffe 2014; Pedoja et al. 2011, 2014). Such sequences consist of "stacked" successive fossil shorelines represented by landforms such as marine terrace (erosional, depositional, and constructional) and notches (Pedoja et al. 2011;

Murray-Wallace and Woodroffe 2014). The fossil shorelines can be well individualized, compound or present as rasa. Compound marine terraces correspond to a succession of two fossil shorelines for which the cliff separating them is reduced, lower than the cliff separating two well-individualized strandlines. Rasas are sequences of terraces, generally erosional (fossil rocky shore platform) wherein shoreline angles are not discernible (Pedoja et al. 2014 and reference therein). Rasas were well defined by Guilcher (1974) who distinguished two morphological types of rasas in function of theirs junctions toward the continent: those limited by an elevated cliff or scarp and those limited by a lower cliff or scarp or even no noticeable break of slope. He assumed the strandflats to be high-latitude rasas where gelifraction and post-Holocene glacial isostatic adjustment (GIA) are important shaping factors, and he associated the planation surfaces of the rasas or strandflats to be created, over a long time by a mixture of repeated marine erosion and continental phenomenon. Pedoja et al. (2014) made the correlation between the Cenozoic sea-level trends and coastal staircase morphology. The staircase shaping of coasts increased during the Pliocene and Pleistocene as a consequence of the intensification of eustatic sea-level oscillations, as inferred from the isotopic record (Lisiecki and Raymo 2005). The formation of rasas was therefore promoted before and during early Pleistocene times, during periods of faster oscillations and lower amplitudes in sea-level fluctuations than since the Middle Pleistocene. At many coastal sites, there is a slight difference between the lower part of the sequence that formed during the Holocene to middle Pleistocene as individualized strandlines and/or compound terraces as compared to the upper part (rocky or sedimentary rasa) (Pedoja et al. 2014). These raw morphological differences between the lower and upper part of the sequence is an asset to explore the lateral continuity of individual shorelines.

The interpretation of Upper and Middle Pleistocene fossil shorelines, such as marine terraces, as being formed during separated highstands of interglacial stages correlated with marine oxygen isotopic stages and/or substages (MIS or MISS) (James et al. 1971; Chappell 1974; Bull 1985; Ota, 1986) is now widely applied to coastal sequences. Each marine terrace is characterized by its shoreline angle, i.e., the angle between the fossil marine abrasion platform and the associated paleo sea-cliff. The shoreline angle of a terrace represents the maximum extension of a transgression and therefore an indicator of sea-level highstand. This correlation of the shoreline with a known highstand in sea level allows the quantification of mean coastal uplift rates. On the field, generally only the inner edge (i.e., the terrace surface next to the shoreline angle) of the terrace is accessible, the shoreline angle being tapped, buried, and/or eroded (e.g., Lajoie 1986).

We mapped and determined the elevations of shoreline angles and inner edges on the field with the use of barometric altimeters (48 sites), and we have correlated them step by step when necessary (vegetation, access) using 2.5-m-resolution SPOT satellite images and 20-m-resolution SPOT DEM extracting the slope images in order to highlight topographic breaks associated with fossil shoreline. The margins of error in the shoreline angle and/or inner edges elevations include the uncertainties associated with their measurement on the field (eroded, tapped) or the DEM vertical resolution and with slope evolution processes.

To chronologically frame the study coastal sequence, we dated 6 samples of mollusk shells by U/Th decay method applied on samples of mollusk shell (Table 1). U-series determination of shells samples was carried out at GEO-TOP research centre of the University of Quebec at Montreal. A piece of few grams of the shell was cut using an abrading device (Dremel® rotary tool). The external layer of the sample was removed in order to reduce the risk of contamination by ^{230}Th-bearing detrital particles. The sample was then burn in a clean crucible in order to destroy organic matter then dissolved with a 7 N HNO_3 in Teflon beakers, and a known amount of spike (^{233}U, ^{236}U, and ^{229}Th) was added to determine U and Th isotopes by isotope dilution technique. To this solution, around 15 mg of Fe carrier was added. In order to concentrate the U and Th elements from the bulk solution, a $Fe(OH)_3$ precipitate was created by adding a solution of ammonium hydroxide until obtaining a pH between 7 and 9. The precipitate was recovered by centrifugation and then dissolved in 6 M HCl. The U–Th separation based on Edwars et al. (1987) was conducted using AG1X8 anionic resin bed. The Th and U-Fe fractions were retrieved by elution with 6 N HCl and H_2O, respectively. The purification of the U fraction was done using 0.2 ml U-Teva (Eichrom® Industries) resin volume. The U-Fe separation was performed by elution using 3 N HNO_3 (Fe fraction) and 0.002 N HNO_3 (U fraction). The purification of Th was performed by elution using a 2 ml AG1X8 resin in 7 N HNO_3 and elution with 6 N HCl. A final purification of Th was carried out on a 0.2-ml AG1X8 resin in 7 N HNO_3, and Th was eluted with 6 N HCl. The U and Th fractions were deposited on Re filament between two layers of graphite and measured using a VG-sector mass spectrometer (TIMS) fitted with an electrostatic filter and a Daly ion counter. Mass fractionation for U was corrected by the double-spike ^{236}U/^{233}U (1.132), while mass fractionation for Th was considered negligible with respect to analytical error. The overall analytical reproducibility, as estimated from replicate measurements of standards, is usually better than 0.5 % for U concentration and ^{234}U/^{238}U ratios and ranges from 0.5 to 1 % for ^{230}Th/^{234}U ratios (2-sigma error range).

Table 1 Summary of dated samples, assigned marine isotopic stages, total displacements, and uplift rates of the marine terraces. Samples 4 and 21 are bivalve shell inlayed at the hardened surface on top of a metric-scale shelly sandstone unit. Sample 10 is a bivalve shell inlayed in a ~2-m-high indurated shelly sandstone unit with conglomerate levels. Sample 11 is a bivalve shell sampled in a metric-scale sandy limy and coquina unit. Sample 33 is a bivalve shell inlayed in a ~3-m-high shell sandstone unit with large pebbles. Sample 48 is a bivalve shell inlayed in a ~5-m-high shelly sandstone unit compounded of numerous shells

Samples	$[^{238}U]$ ppb	$[^{232}Th]$ ppb	$(^{234}U/^{238}U)$	$(^{230}Th/^{234}U)$	$(^{230}Th/^{232}Th)$	Age (yr)	Marine terrace	Assigned MIS stage	MIS age (ka)	Shoreline angle elevation (m)	Sample elevation	Longitude (E)
4	519.3834 ± 2.0846	2.346 ± 0.0103	1.2228 ± 0.0129	0.4691 ± 0.0072	388.11 ± 4.912	67,305 (+1484/−1458)	T1	MIS 5e	124 ± 8	3.5 ± 1	3.5 ± 1	247.625
								MIS 3	48 ± 16			
10	408.3834 ± 4.3802	175.7923 ± 0.9591	1.0976 ± 0.0159	1.1784 ± 0.0192	9.183 ± 0.130	Outside age	T4	>MIS 11		47 ± 10	43 ± 10	2.50047
11	1090.8858 ± 4.4087	3.2483 ± 0.0150	0.9886 ± 0.0094	1.0805 ± 0.0142	1096.340 ± 11.920	Outside age	T6	>MIS 11		82 ± 10	80 ± 10	2.49589
21	2037.3721 ± 11.2445	3.5935 ± 0.0486	1.3781 ± 0.0135	0.6334 ± 0.0103	1512.514 ± 29.555	102,636 (+2824/−2745)	T1	MIS 5 c	105 ± 5	7 ± 1	5 ± 1	2.67075
21								MIS 5e	124 ± 8			
33	403.7319 ± 1.4767	4.416 ± 0.0195	1.1189 ± 0.0069	1.0112 ± 0.0084	316.090 ± 2.509	394,799 (+41,801/−30,275)	T3	MIS 11	390 ± 30	63 ± 10	55 ± 10	2.81028
48	889.1960 ± 6.4588	8.3350 ± 0.0714	1.2908 ± 0.0172	0.7248 ± 0.0121	305.044 ± 4.589	130,466 (+4466/−4260)	T1	MIS 5e	124 ± 8	8 ± 3	7 ± 3	2.90668

Samples	Latitude (N)	Sea-level highstand[a] elevation (m)	Sea-level highstand[b] elevation (m)	Sea-level highstand[c] elevation (m)	Sea-level highstand[d] elevation (m)	Sea-level highstand[e] elevation (m)	Apparent uplift rate (mm/yr)	Uplift rate[a] (mm/yr)	Uplift rate[b] (mm/yr)	Uplift rate[c] (mm/yr)	Uplift rate[d] (mm/yr)	Uplift rate[e] (mm/yr)
4	36.62183	1 ± 1	5 ± 2	5.25 ± 3.75	2 ± 1	6 ± 4	0.03 ± 0.01	0.02 ± 0.02	−0.015 ± 0.025	−0.02 ± 0.04	0.01 ± 0.02	−0.025 ± 0.045
10	36.58872					−65 ± 15	0.09 ± 0.05					1.69 ± 0.95
11	36.58359											
21	36.63582	−35 ± 15	−21.5 ± 16.5				0.41 ± 0.17	0.28 ± 0.18		0.05 ± 0.02		
21	36.63582	1 ± 1	5 ± 2	5.25 ± 3.75	2 ± 1	6 ± 4	0.06 ± 0.01	0.05 ± 0.02	0.015 ± 0.025	0.015 ± 0.045	0.04 ± 0.02	0.01 ± 0.04
33	36.68735	−1 ± 1	−2 ± 1			5 ± 5	0.165 ± 0.035	0.17 ± 0.04	0.17 ± 0.04			0.15 ± 0.05
48	36.8055	1 ± 1	5 ± 2	5.25 ± 3.75	2 ± 1	6 ± 4	0.065 ± 0.025	0.055 ± 0.035	0.025 ± 0.045	0.025 ± 0.055	0.055 ± 0.035	0.02 ± 0.06

[a] According to Bintanja et al. (2005)

[b] According to Siddall et al. (2006)

[c] According to Hearty et al. (2007)

[d] According to Bardají et al. (2009) and Dorale et al. (2010)

[e] According to Murray-Wallace and Woodroffe (2014)

The U-series disequilibrium results are shown in Table 1. However, the dating results were used to correlate the shoreline of each dated terrace with highstand, whose age is known from literature (e.g., Bintanja et al. 2005; Siddal et al. 2006). Our sampling strategy consisted of trying to date the lowstanding terraces and associated deposits (purported the youngest) because higher (i.e., older) terrace have ages beyond the limit of the *U*/Th method.

We calculate uplift rates with and without correction for eustasy. The mean uplift rate (*U*) is calculated by using the following equation (e.g., Lajoie 1986):

$$U = (E - e)/A.$$

with (*E*) the present-day elevation of the inner edge (or shoreline angle) of the terrace, (*e*) the paleo-elevation of each shoreline (i.e., eustatic component) which may corresponds to either the eustatic (ice-equivalent) sea level reached during the interglacial (e.g., MIS 5e) or interstadial (e.g., MIS 3), (*A*) the age of the associated interglacial or interstadial stage.

We also compute apparent uplift rates (Ua) as Ua = *E*/*A*, i.e., rejecting any a priori correction for eustasy (e) as in Pedoja et al. (2011, 2014). Errors reported on both computed uplift rates include uncertainties in the MIS ages and shoreline angle altitude measurements.

Global estimates of last interglacial sea levels include many controversial issues. For example, the sea level of last interglacial maximum (MIS 5e) is "traditionally" described as reaching +6 m APSL (above present sea level) or even more (e.g., up to 9 m see Hearty et al. 2007; Kopp et al. 2009; Dutton and Lambeck 2012; Creveling et al. 2015). But this point is debated (Pedoja et al. 2011, 2014; Murray-Wallace and Woodroffe 2014).

Consequently, as in Murray-Wallace and Woodroffe (2014), we consider that, most probably, 1) MIS 5e sea level (124 ± 8 ka) was between +2 and +10 m higher than present (6 ± 4 m); 2) MIS 7 sea level (217.5 ± 27.5 ka) was−3 ± 3 m lower than present; and 3) MIS 9 (324.5 ± 18.5 ka) was similar to present (0 ± 2 m) 4), whereas MIS 11 (390 ± 30 ka) was probably higher than present by 5 ± 5 m (Fig. 4). These synthetic values correspond to the mean (with associated margin of error) of the observed ranges (both in age and in eustasy). Few studies provide information on interglacials older than MIS 11, and uncertainties in their timing, duration, and number of highstands are large.

In order to illustrate the various results (and perplexity in interpretation, see Caputo 2007) brought by the use of different ages and correction for eustasy, we calculate our upper and Middle Pleistocene uplift rates (Table 1) using the data from more deterministic (Bintanja et al. 2005; Siddall et al. 2006; Hearty et al. 2007) or regional studies (Bardaji et al. 2009; Dorale et al. 2010).

Nevertheless, to tentatively estimate the onset of coastal uplift record through the formation of a coastal sequence and to propose an age for the highest coastal indicators (purported the oldest), (1) we extrapolated our Middle Pleistocene uplift rates, (2) we analyzed the spatial relationships between marine terraces/rasas and the geological markers already recognized in the studied area, (3) we used sea-level referential data (Haq et al. 1987; Lisiecki and Raymo 2005; Miller et al. 2005; Kominz et al. 2008) and bibliographical data of Mediterranean sea-level records to correlate these geomorphological surfaces with old, "large temporal wavelength" highstands.

Geomorphic indices

Morphometric parameters were extracted from the river network and topography of the 20-m-resolution SPOT DEM using Rivertools and Arcgis softwares. This morphometric analysis highlights changes in tectonic uplift by taking into account the influence of lithology and excluding the impact of the climate since it is the same throughout the relatively small studied area (600 km^2). Similar studies were already conducted in coastal California (Merritts and Vincent 1989; Snyder et al. 2000, 2003; Duvall et al. 2004) and recently in Indonesia (Nexer et al. 2015) where authors correlated morphological properties of drainage basins with uplift rates (e.g., channel length, gradient and width, basin area, relief, drainage density, steepness index ksn, shape factor, hypsometric integral).

We decide to use the morphometric indices which correlate with the uplift rate in the specific conditions corresponding to coastal streams draining marine terraces: the basin elongation ratio and the hypsometric integral (Nexer et al. 2015).

The basin elongation ratio (Re) represents the elongation of a catchment and is calculated through the following equation (Schumm 1956):

$$Re = (2\sqrt{A}/\sqrt{\psi \psi})/L_B$$

where L_B is the maximum basin length and *A* is the catchment area. We use this parameter because in an uplifting landscape, drainage basins tend to be elongated.

The hypsometric integral (HI) represents, for a watershed, the distribution of elevation as a function of the drainage area in a watershed (Strahler 1952; Mayer 1990; Keller and Pinter 2002). It is calculated with the following equation.

$$HI = (El_m - El_{min})/(El_{max} - El_{min})$$

where El_m is the mean elevation, E_{max} the maximum elevation, and E_{min} the minimum elevation. *HI* can be viewed as the fractional volume of a basin that has not yet been eroded.

HI is an indicator of landscape evolution influenced by forcing factors (i.e., tectonics, climate, lithology) on topography (Hurtrez et al. 1999). More precisely, HI is related to the degree of dissection of a basin. Consequently, it indicates the relative dominance of incision and hillsope processes in landscape evolution. The parameter is strongly sensitive to the drainage area especially when the steady-state topography is not reached (Hurtrez et al. 1999; Cheng et al. 2012). To remove these effects, we only consider watersheds with the same Strahler order (SH = 5) (Strahler 1952), as advised by Cheng et al. (2012) (a SH = 1 drain is defined as draining a minimum area of 1400 m^2).

Results

Coastal sequences analyses

Distribution of the Sahel ridge marine terraces and rasas

We surveyed the coast from El Marsa (in the Chlef Province) to Ain Taya (Algiers Province) (Fig. 1a) and observed sequences of fossil shorelines (wave-cut and/or wave-built terraces and sometimes rasas) over a 220-km-long stretch of coast.

Along a ~70-km-long coastal area, Late Cenozoic coastal morphologies and deposits are found on the northern flank of the Sahel ridge between the Chenoua and Algiers massifs (Fig. 1b). On the latter massif, the sequence reaches a maximum elevation of ~370 ± 20 m. Between the Chenoua and the Algiers massifs, the staircase coastal morphologies of the northern flank of the Sahel ridge reveal a sequence of paleo-shorelines conform to the present-day shoreline (Fig. 2a); the fossil shorelines underline a 50-km-long embayment-orientated SW–NE. All along this coastal stretch, the middle and upper shorelines constituting the sequence (i.e., T3 to T10) are laterally continuous except in the Mazafran valley where the sequence is eroded by the river. The lower shorelines can underline smaller embayments (T1 and T2) and/or be covered by aeolian deposits. Nevertheless, the lateral continuity of the lower shorelines is proved by their morphology and topographic position. On the southern flank of the Sahel ridge, we also observed extensive outcrops of coastal deposits (Fig. 3a) but without clear staircase morphology. This lack might result from less efficient coastal erosion in this protected area, the submerged Mitidja plain forming a ria.

The coastal sequence located west of Algiers is subdivided into a lowstanding sequence of marine terraces (Fig. 3b) overlooked by widespread rasas (up to 6). The "Tombeau de la Chrétienne" monument is built on the T7 upper rasa that forms the top of the Sahel ridge (Fig. 3c, see Fig. 2a for location). T6 rasa presents a metric-scale petrocalcic horizon (Fig. 3d). For the lower part of the sequences (identified shorelines), the coastal deposits and morphologies reside in "typical" marine terraces (i.e., fossil rocky shore platform with typically less than 1 meter of coastal deposit), but locally (i.e., inland from Sidi Ferruch tombolo, see Fig. 2a for location) the terraces are covered by several meters of sandy coastal deposits and resemble "wave-built" terraces (Fig. 3e). These lowstanding deposits and morphologies are frequently covered or capped by aeolian deposits, but morphological differences between the lower and upper parts of the sequence allow us to explore the lateral continuity of individual strandline.

We performed five altitudinal transects and measured 48 elevations of fossil shorelines (Fig. 2a, b). The sequence of marine terraces and rasas reaches a maximum altitude of 370 ± 20 m (Profile AT5) and includes up to 10 main fossil shorelines, west and east of the Mazafran valley (Profil AT2-2′, AT3, AT5 in Fig. 2b). Compared to previous studies (Saoudi 1989; Maouche et al. 2011), we describe two or three supplementary fossil shorelines, east and west of the Mazafran valley, respectively. The topographic profiles along the flat surfaces associated with T7, T5, and T3 fossil shorelines evidence a continuous eastward increase in their elevations (Fig. 2a, c). For the westernmost part of the profiles, we calculated the inclination of T7, T5, and T3 surfaces (i.e., their angle from the horizontal, see Fig. 2c: This angle is higher for the highest (i.e., oldest) rasas and terraces). East of the Mazafran valley, elevations of the same fossil shoreline are still almost constant. Over this 20-km-long stretch of coast, T3, T5, and T7 are located, respectively, at 55 ± 10 m, 135 ± 20 m, and 250 ± 20 m (Fig. 2c).

Chronostratigraphy and uplift rates

We dated by U/Th method six samples (shells of bivalve) from six sites (Fig. 2a; Table 1) outcropping on the low-standing terraces, respectively T1 (three samples: 4, 21, 48), T3 (one sample: 33), T4 (one sample: 10), and T5 (one sample: 11). Samples 4, 21, and 48 taken in T1 deposits yielded ages of 67.3 ± 1.5 ka on Chenoua transect. 102.6 ± 2.8 ka on Bou Haroun transect, and 130.4 ± 4.4 ka on Ain Benian transect.

Samples taken in T1 deposits on different sites along the Algiers shores yielded different ages that can lead to different interpretations: (1) Sample 4 suggests a possible correlation with a sea level during MIS 3 (~32–64 ka in Murray-Wallace and Woodroffe, 2014) an interstadial characterized by "low" sea levels (<−50 m) (Murray-Wallace and Woodroffe 2014) or even to the lowstand associated with MIS 4 (~60–75 ka), (2) sample 21 suggests a correlation with MIS 5c (~105 ka), a highstand following last
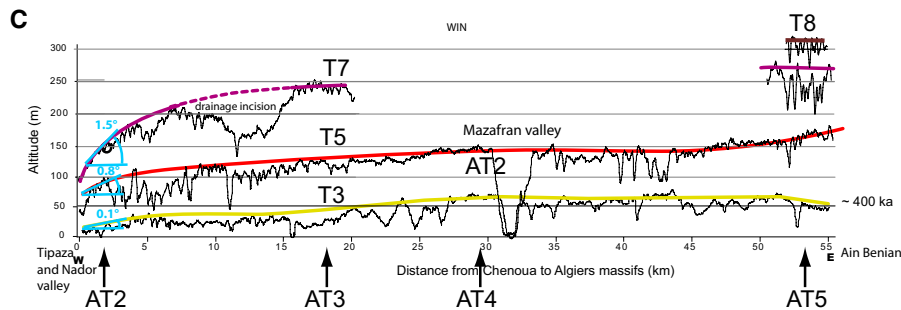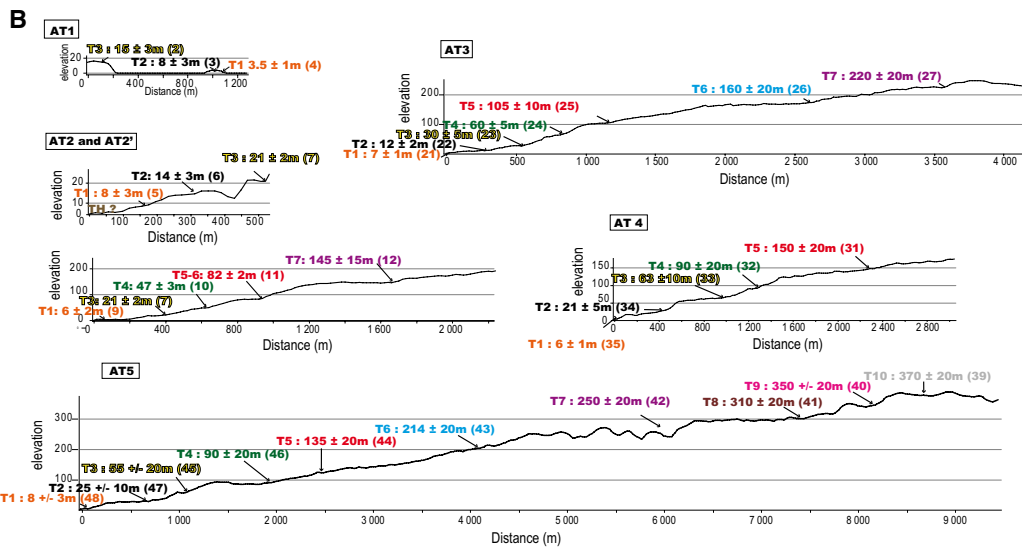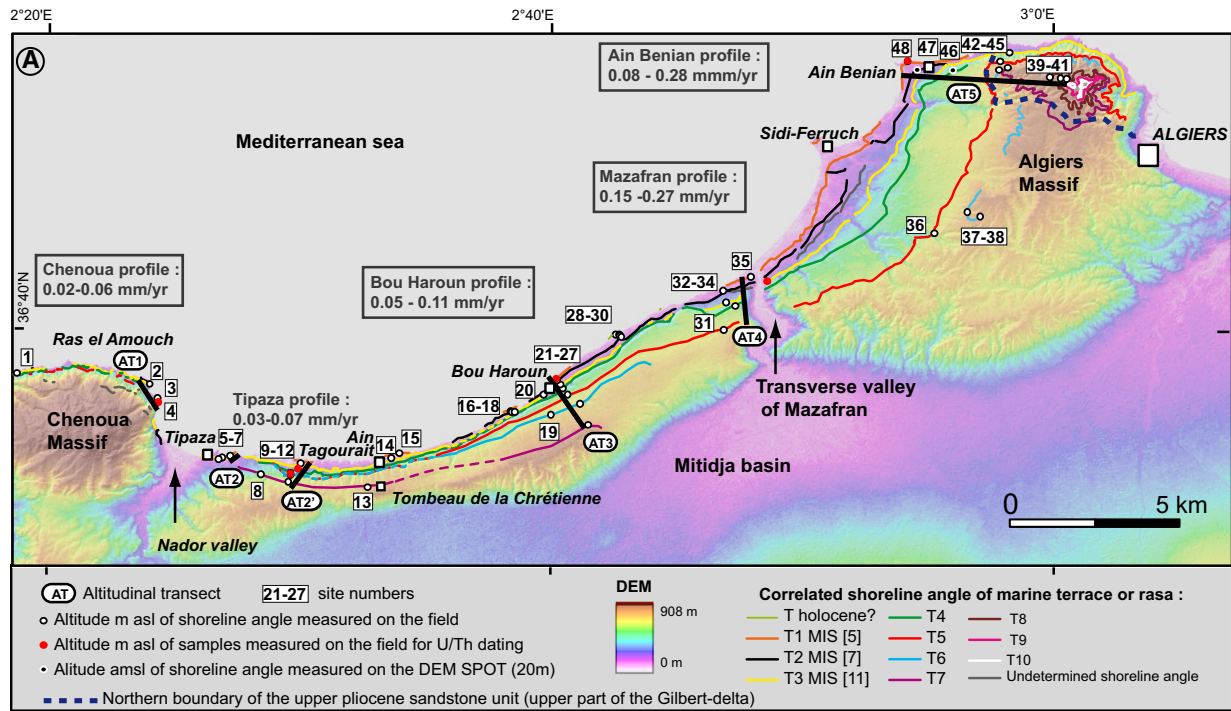
Fig. 2 Sequence of marine terraces and rasas on the northern flank of the Sahel ridge. **a** Distribution **b** elevation transects and interpretation profiles. *Site numbers* are indicated in brackets. **c** Topographic profiles (*black line*) and covered surfaces of the *T3, T5*, and *T7 shore-lines* (*colored lines*) from Tipaza to Ain Benian. *Blue* values are the westward tilt values in degree for each shoreline. *Black arrows* indicate the location of altitudinal transects of Fig. 2b
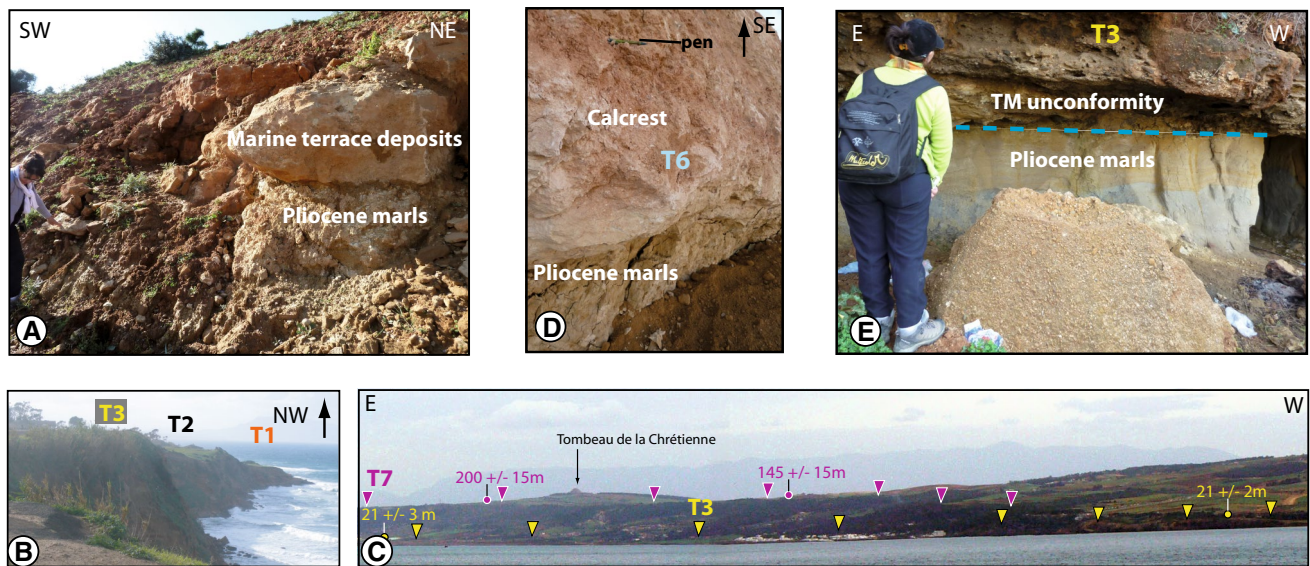
Fig. 3 The coastal sequence on field. For location, see Fig. 1b. **a** *Picture* showing marine terrace deposits lying on Pliocene sandstones on the southern limb of the *Sahel ridge* indicating the incursion of the sea in the Mitidja basin during Pleistocene times. **b** Interpreted picture of the site showing the lower part of the sequence (*T*1, *T*2, and *T*3) east of Bou Haroun. **c** Interpreted picture (view looking south-east) showing the tilting of *T*7 in the landscape of the southwestern part of the Sahel ridge. **d** Interpreted picture looking southeast showing the coastal deposits of *T*6) affected by petrocalcification. **e** Interpreted picture showing the discordance between marine terrace deposits (*T*3) and Pliocene marls

interglacial maximum (MIS 5e), and (3) sample 48 suggests a correlation with MIS 5e (~120 ka).

At this stage of the study, we discard hypothesis 1 (*T*1 = MIS 3 or even MIS 4) because (1) coastal landform or deposit related to lowstands have not been dated in any emerged sequence around the world even if, in case of long lasting uplift, such lowstand features should theoretically emerge (e.g., Pirazzoli et al. 1993). (2) Sequence including MIS 3 terraces are generally including an overlooking MIS 5e terrace (see Figure 10 in Pedoja et al. 2014) and there are generally a couple or more terraces associated with the MIS 3 sea levels, what is not the case on the Chenoua coasts. (3) Fossil shoreline associated with the sea levels that occurred during MIS 3 are present on coasts experiencing high uplift rates (>0.5 mm/year in Murray-Wallace and Woodroffe 2014 and 1.18 ± 0.08 mm/year in Pedoja et al. 2014). (4) U/Th results on the deposits from the same terrace (i.e., *T*1 samples 21 and 48) are not consistent with such an age.

The young U/Th age yielded by sample 4 may probably be either a consequence of contamination of the sampled shells by post-diagenetic uranium because the (^{234}U/^{238}U) ratio of 1.22 is higher than expected for a marine shell evolving in a closed system [(^{234}U/^{238}U) ≤ 1.15], or due to the sampling of a shell inlayed in the hardened surface on the top of the terrace that could have be formed after the terrace formation (Table 1). Given the result of samples 21 and 48, *T1* fossil shoreline was surely carved

during last interglacial period (i.e., MIS 5), but, as said above, this ages could relate to two different highstands during this period: MIS 5e or MIS 5c. Sample 21 gives an age associated with MIS5c but could be associated with MIS5e if we considered an underestimated dating induced by an open radioactive system [(^{234}U/^{238}U) ratio of 1.378] or by the sampling at the updated terrace surface as for sample 4.

We emphasize here that the chronostratigraphical interpretation consists in correlating the shoreline with a known highstand not the deposits present on the terrace. In fact, these deposits could have occurred during a later highstand in sea level than the one which carved the shoreline. More dating are needed to address fully this question. At this stage, we tentatively correlate *T*1 shoreline with the last interglacial maximum (MIS 5e) and we propose that *T*1 deposits may include deposits associated with MIS 5c (and 5a?) (i.e., compound terrace). This interpretation is in agreement with dating of the *T*3 deposits (i.e., *T*3 = MIS 11) and previous dating and chronostratigraphical interpretation of the lower part of the sequence (Stearns and Thurber 1965; Saoudi 1989). Furthermore, it seems to be, apparently, the more realistic as MIS 5a, 5c sea level are considered as lower (or subequal) to the sea level during MIS 5e (Murray-Wallace and Woodroffe 2014). Consequently due to the uplift, MIS 5e highstand should have been preserved from coastal erosion during MIS 5c and 5a, but the latter stands were probably efficient relatively
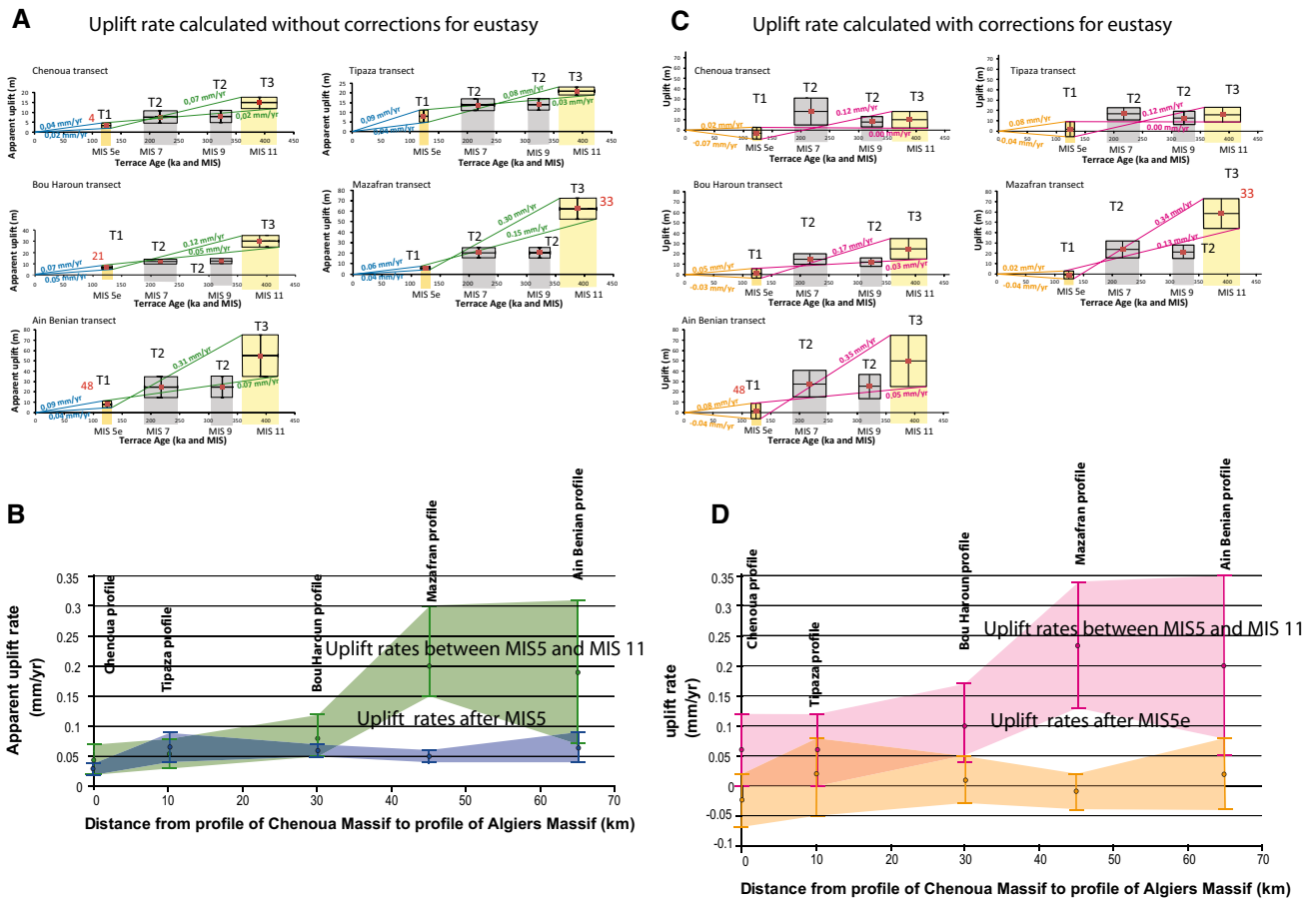
Fig. 4 Uplift rates calculated according to the dating of terraces $T1$ and $T3$. **a** Estimated apparent coastal uplift rates (transects located on Fig. 2a) since 120 ka (*blue values*) and between 120 to 400 ka (*green values*) using the ages, elevations, and uncertainties associated with $T1$ and $T3$. We propose a correlation of $T2$ with the MIS 7 and/or MIS 9 stages. **b** Alongshore SW–NE variation of the apparent uplift rates since 120 ka (*in blue*) and between 120 and 400 ka (in green) determined on $T1$ and $T3$ marine terraces (MIS 5e and MIS 11, respectively). Points represent mean value of uplift rate for each transect. **c** Estimated coastal uplift rates transects located on Fig. 2a)

since 120 ka (*blue values*) and between 120 to 400 ka (green values) using the ages, elevations, and uncertainties associated with $T1$ and $T3$, and corrections for eustasy according Murray-Wallace and Woodroffe (2014). We propose a correlation of $T2$ with the MIS 7 and/or MIS 9 stages. **d** Alongshore SW–NE variation of the uplift rates estimated with correction for eustasy since 120 ka (*in orange*) and between 120 to 400 ka (*in pink*) determined on $T1$ and $T3$ marine terraces (MIS 5e and MIS 11, respectively). Points represent mean value of uplift rates for each transect

to the carving of $T1$ platform or responsible for some of the deposits now preserved on $T1$.

Sample 33 taken in $T3$ deposits yielded an age of 394.8 ± 41.8 ka, close to the limit of the U/Th method. According to this dating, we tentatively correlate the shoreline angle of $T3$ with a highstand assigned to MIS 11 (400 ± 20 ka). Samples 11 and 10 taken, respectively, in $T4$ and $T5$ deposits both yielded ages outside of the dating range of the U/Th decay method. It probably implies that $T4$ and $T5$ shorelines were carved during highstands older than MIS 11.

Consequently, we propose the following chronostratigraphy. $T1$ (whose elevation ranges from 3.5 ± 1 m to 8 ± 3 m) was carved during maximum of the last interglacial MIS 5e, and $T3$ whose elevation ranges from 15 ± 3 m

to 55 ± 10 m was carved during the highstand associated with MIS 11 highstand (400 ± 20 ka). These previous correlations imply that $T2$ could be correlated with highstands during MIS 7, MIS 9, or both. A linear extrapolation of the mean apparent or corrected for eustasy uplift rate does not strictly favor a correlation with MIS 7 or with MIS 9 (Fig. 4a, c). More dating are needed to fully address this outstanding question.

The net vertical displacements and associated uplift rates for each site of dated marine terraces, which include mean uplift rates calculated with or without correction for eustasy, are given in Table 1. Uplift rates are calculated also for two different time intervals: since 120 ka (MIS 5e) and between 120 and 400 ka (MIS 11) for the five profiles along the coast, assuming a constant uplift rate between

highstands and taking into account elevation and age uncertainties (Fig. 4a, c). Mean apparent uplift rates and corrected uplift rates since 120 ka are globally steady all along the coast with a mean value of 0.055 ± 0.015 mm/year (apparent) and of 0.005 ± 0.045 mm/year (corrected for eustasy). Between 120 and 400 ka mean, uplift rates are increasing eastward, wherever they are apparent (increase from 0.045 ± 0.025 to 0.19 ± 0.12 mm/year) or corrected (0.06 ± 0.06 to 0.2 ± 0.15 mm/year) (Fig. 4b, d). Uplift rates between 120 and 400 ka located to the west (Chenoua and Tipaza transects) are similar with uplift rates integrated since 120 ka (Fig. 4b, d). Values of uplift rates between 120 and 400 ka in the eastern zone are higher than those calculated since 120 ka (Fig. 4b, d). The spatial variation of uplift rates between 120 and 400 ka agree with the spatial changes of finite uplift for older terraces and rasas (T5 and T7) increasing eastward (Fig. 2c). The uplift rates calculated between 120 and 400 ka are consequently better representative of the long-term tectonic pattern than those calculated since 120 ka. Significantly smaller uplift rates since 120 ka may indicate either a quiescence or the ending of folding.
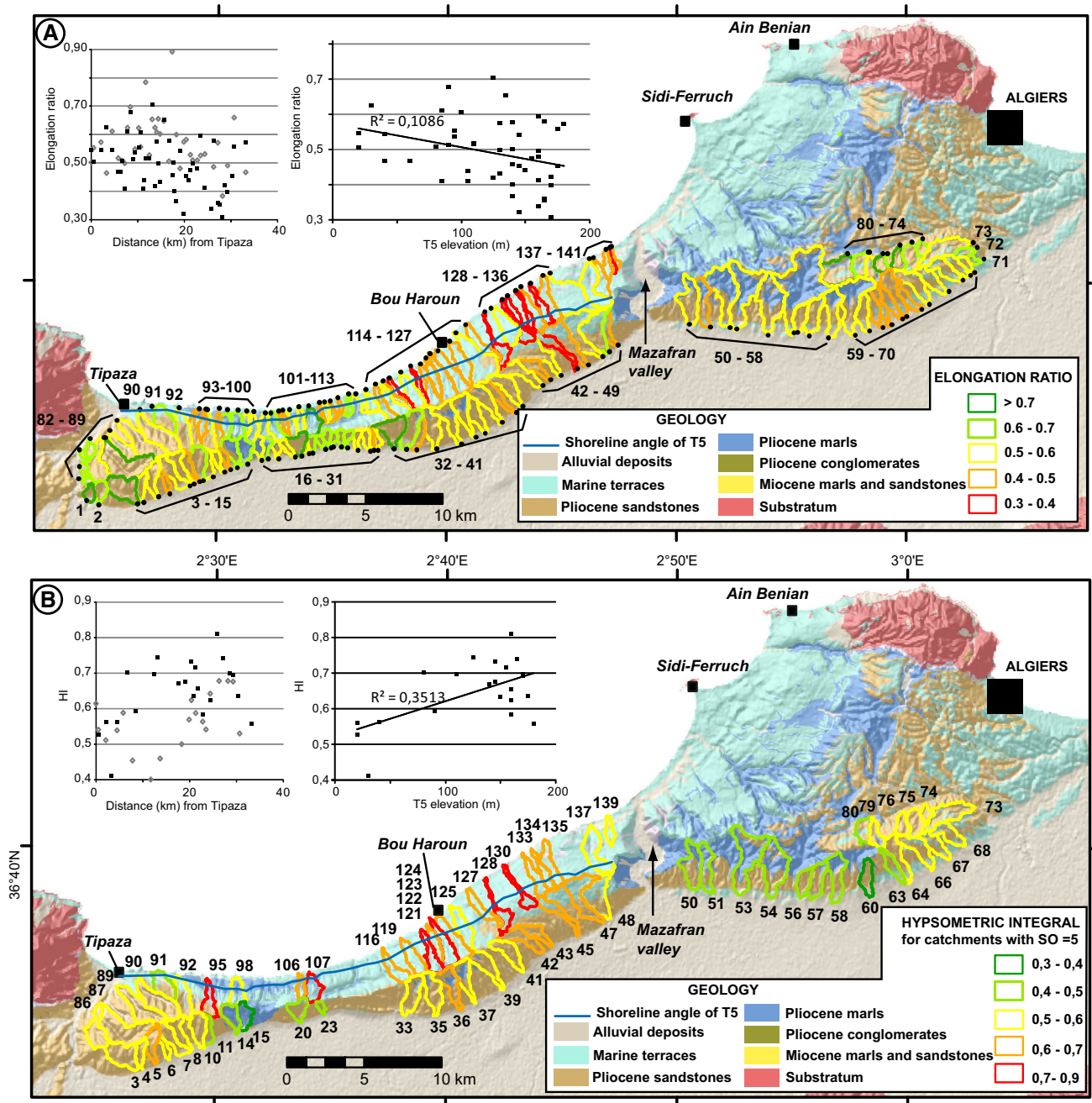
Morphometric analyses

Re and HI values for basins along the Algiers and Sahel reliefs are presented in Fig. 6a, b, respectively. We also added plots of morphometric values of the northern and southern Sahel flank catchments versus distance from Tipaza to Mazafran River in order to compare the morphology of the two flanks (Fig. 6a, b). Finally, we produced plots showing the morphometric values of the northern Sahel flank catchments versus uplift of T5 marine terrace in order to analyze the potential linear correlation between these parameters. Re indices were calculated for 141 basins extracted from the 20-m-resolution SPOT DEM (Fig. 5a; Table 2). The values range from 0.31 to 0.89. The difference between the values of Re for the northern and southern Sahel flank catchments highlights an asymmetry between the two sides of the Sahel ridge (Fig. 5a). On the southern flank of the Sahel ridge, Re values are higher than on the northern flank, indicating that the northern basins are more elongated. Longitudinally, we detect high-to-moderate values (0.5 < Re) in the E-trending western Sahel termination (basins no. 1 to 35 and 82 to 114), low-to-moderate values (0.3 < Re < 0.5) in the NE–SW-trending central Sahel part (basins no. 36 to 49 and 115 to 141), and globally low-to-moderate values for catchments east of the Mazafran valley except for basins n° 61 to 65. The relationship between Re values of northern catchments and uplift of the T5 rasa is inferred (Re versus uplift graph of Fig. 5a). We detect a global slight decrease in the Re values when uplift increases but without clear correlation.

Hypsometric integrals were computed for 67 basins with a 5-Strahler order (Fig. 5b; Table 2). The values range from 0.39 to 0.8. We separate the basins into four classes of HI values. West of the Mazafran valley, on the southern flank of the Sahel ridge, hypsometric integrals present lower values than those on the northern flank (Fig. 5b). Longitudinally, we roughly divide the western Sahel into two parts with moderate HI values (0.4 < HI < 0.6) in the E-trending western Sahel termination (basins n°3 to 23 and 86 to 107) and high values (0.6 < HI < 0.9) in the NE–SW-trending Sahel part (basins n°33 to 48 and 116 to 139). East of the Mazafran valley, we determined two ranges of HI values: a range of low values (0.5 < HI) for watersheds located in the central part (basins n° 50 to 60) of the southern fold of the Algiers massif and a range of moderate values (0.5 < HI < 0.6) for watersheds located in its eastern part (basins n°63 to 80). The hypsometric integral versus uplift graph of Fig. 6b presents the relationships between HI values of the northern catchments and the uplift of T5 rasa. The linear correlation between the two parameters is not good, but generally low uplift rates deduced from T5 elevation are associated with low HI values, whereas higher uplifts rates deduced from T5 elevation are associated with higher HI values.

Geological data

On the northern flank of the Sahel ridge, two outcrops of marls under marine terrace deposits strata allowed us to measure the strata direction and dip (Fig. 1b). The directions are N45° and N67° and the dips are 22° and 20° to the SE, for the sites 1 and 3, respectively (Figs. 1b, 6). According to the neighboring Mazafran cross section (Aymé et al. 1954; Yassini 1975) and regional Tipaza-Kolea 1:50,000-scale geological maps (Aymé et al. 1962; Ficheur and Jacob 1911), measured strata of site 3 correspond to Upper Miocene marls, whereas westward, measured strata of site 1 are associated with Lower Pliocene marls. No Upper Pliocene sandstones strata outcrop of the northern flank of the Sahel ridge. The marine deposits lay directly above the Lower Pliocene marls (Fig. 3d, e). On the southern flank of Sahel, we measured the direction and dip of the Upper Pliocene sandstones strata at two other sites (sites 2 and 4, Fig. 1b). As for sites 1 and 3, we identified and quantified a southward dipping (62° to the S and 31° to the SE, for sites 2 and 4, respectively) in agreement with a monoclinal structure of the onshore Sahel ridge (Fig. 6). To determine the offshore extension of the structure, we added to the NW–SE cross sections of Fig. 6 and interpreted seismic profiles from Yelles et al. (2009) and Strzerzynski et al. (2010). To connect the offshore geological strata with the onshore geological formation exposed in the outcrop sites of this study and the eastern flank of the Mazafran valley

Fig. 5 Morphometric parameters values for basins along the Algiers and Sahel reliefs, plot of morphometric values versus the distance of the northern and southern Sahel flank catchments from Tipaza and linear correlations between values of morphometric indices and elevation of *T*5 marine terrace used as a proxy of uplift. In the morpho-metric values versus distance plots, black squares and white circles correspond to catchments located, respectively, on the northern and southern flank of the ridge. **a** Elongation ratio. **b** Hypsometric integral values for catchments of Strahler order of 5. These data are represented on the geological map

cross section (Aymé et al. 1954), we used the lithological data of the Algiers borehole (Burollet et al. 1978) of 1200 depth located across the MS5 profile (Figs. 1, 6). The seismic profiles have highlighted neighboring offshore anticline. The southeastward part of the MS5 seismic profile in Yelles et al. (2009) allows to visualize the offshore northern flank of the Sahel fold.

Discussion

Proposed Late Cenozoic chronostratigraphy

The most complete sequence of strandlines (AT5, Fig. 2a, b) is located west of Algiers, where 10 successive terraces and rasas are observed between the modern shoreline and

Table 2 Selected catchments and values of morphometric indices

Basin number	Re	HI	Strahler order	Area (km^2)
1	0.76	0.42	4	0.63
2	0.68	0.55	4	0.97
3	0.72	0.51	5	2.68
4	0.51	0.55	5	0.89
5	0.50	0.61	5	1.38
6	0.49	0.54	5	0.53
7	0.55	0.51	5	1.65
8	0.57	0.55	5	1.42
9	0.46	0.54	4	0.89
10	0.61	0.59	5	1.78
11	0.52	0.44	5	0.84
12	0.51	0.56	4	0.52
13	0.50	0.56	4	0.44
14	0.62	0.45	5	1.40
15	0.70	0.40	5	1.34
16	0.55	0.57	4	0.75
17	0.62	0.52	4	0.61
18	0.59	0.46	4	0.46
19	0.56	0.40	4	0.48
20	0.78	0.46	5	1.25
21	0.53	0.44	4	0.18
22	0.65	0.46	4	0.45
23	0.62	0.47	5	0.32
24	0.61	0.65	4	0.47
25	0.66	0.47	4	0.34
26	0.60	0.47	4	0.47
27	0.65	0.52	4	0.42
28	0.58	0.49	4	0.49
29	0.58	0.51	4	0.57
30	0.46	0.45	4	0.33
31	0.51	0.38	4	0.43
32	0.89	0.56	6	2.21
33	0.60	0.50	5	2.17
34	0.48	0.44	4	0.92
35	0.57	0.57	5	2.14
36	0.58	0.62	5	2.09
37	0.53	0.59	5	1.81
38	0.51	0.47	4	1.49
39	0.51	0.56	5	1.97
40	0.41	0.54	4	1.18
41	0.53	0.54	5	1.86
42	0.53	0.64	5	1.91
43	0.49	0.68	5	1.18
44	0.57	0.77	6	3.41
45	0.38	0.68	5	1.56
46	0.49	0.68	6	2.79
47	0.56	0.68	5	3.25
48	0.66	0.53	5	3.17
49	0.47	0.58	4	0.93

Table 2 continued

Basin number	Re	HI	Strahler order	Area (km^2)
50	0.56	0.45	5	2.78
51	0.48	0.45	5	2.11
52	0.58	0.45	6	4.38
53	0.56	0.45	5	5.02
54	0.59	0.45	5	4.39
55	0.58	0.48	6	9.59
56	0.59	0.42	5	1.30
57	0.55	0.45	5	1.87
58	0.52	0.43	5	2.40
59	0.60	0.52	6	4.20
60	0.55	0.39	5	1.49
61	0.49	0.39	4	1.24
62	0.43	0.44	4	1.05
63	0.44	0.44	5	1.25
64	0.49	0.55	5	2.08
65	0.47	0.38	4	1.02
66	0.52	0.58	5	2.17
67	0.56	0.51	5	1.55
68	0.58	0.56	5	1.70
69	0.52	0.49	4	1.02
70	0.59	0.49	4	0.52
71	0.69	0.57	4	0.34
72	0.61	0.59	4	0.66
73	0.51	0.56	5	2.87
74	0.68	0.53	5	0.62
75	0.69	0.54	5	1.59
76	0.72	0.57	5	1.02
77	0.68	0.50	4	0.36
78	0.84	0.55	4	0.76
79	0.57	0.54	5	1.17
80	0.66	0.46	5	1.28
81	0.84	0.44	6	3.25
82	0.63	0.73	4	0.34
83	0.63	0.60	4	0.35
84	0.61	0.50	3	0.27
85	0.69	0.43	4	0.54
86	0.56	0.56	5	2.27
87	0.73	0.55	5	4.66
88	0.55	0.55	4	1.46
89	0.51	0.53	5	3.02
90	0.55	0.56	5	3.24
91	0.63	0.41	5	1.82
92	0.55	0.56	5	2.09
93	0.47	0.63	4	1.04
94	0.47	0.54	4	0.71
95	0.51	0.70	5	1.39
96	0.41	0.60	4	0.75
97	0.61	0.55	4	0.92
98	0.68	0.59	5	1.39

Table 2 continued

Basin number	Re	HI	Strahler order	Area (km²)
99	0.51	0.54	4	0.53
100	0.54	0.70	4	0.91
101	0.55	0.61	4	1.02
102	0.61	0.55	4	1.18
103	0.41	0.58	3	0.38
104	0.44	0.59	4	0.47
105	0.52	0.69	4	0.73
106	0.52	0.70	5	0.69
107	0.71	0.75	5	1.50
108	0.42	0.69	4	0.25
109	0.58	0.66	4	0.43
110	0.50	0.76	4	0.34
111	0.43	0.72	4	0.29
112	0.65	0.67	4	0.41
113	0.58	0.65	6	4.65
114	0.58	0.75	4	0.72
115	0.46	0.63	4	1.14
116	0.50	0.67	5	1.48
117	0.40	0.70	4	0.57
118	0.37	0.60	4	0.79
119	0.54	0.68	5	1.81
120	0.32	0.67	4	0.61
121	0.45	0.73	5	1.60
122	0.44	0.63	5	1.10
123	0.48	0.72	5	2.11
124	0.50	0.66	5	2.19
125	0.48	0.58	5	2.00
126	0.60	0.63	6	4.28
127	0.41	0.62	5	1.42
128	0.34	0.81	5	1.33
129	0.58	0.66	6	2.19
130	0.36	0.74	5	1.18
131	0.36	0.54	4	0.86
132	0.31	0.65	4	0.68
133	0.42	0.70	5	1.52
134	0.40	0.69	5	1.14
135	0.45	0.64	5	1.85
136	0.56	0.63	6	4.79
137	0.57	0.56	5	2.81
138	0.49	0.57	4	1.48
139	0.49	0.52	5	0.77
140	0.39	0.51	4	0.31
141	0.43	0.47	4	0.32
142	0.50	0.54	6	5.95
143	0.54	0.44	6	9.18
144	0.70	0.55	8	37.56
145	0.37	0.42	6	10.96
146	0.50	0.38	7	11.93
147	0.52	0.50	7	19.50

Table 2 continued

Basin number	Re	HI	Strahler order	Area (km²)
148	0.60	0.45	7	32.62

the top of the Algiers massif at an elevation of 370 ± 20 m. The coastal uplift rates between 120 and 400 ka range from 0.07 to 0.31 mm/year (apparent) and from 0.05 to 0.35 mm/year (corrected for eustasy) (Fig. 4). These new estimates agree with the estimates of Morel and Meghraoui (1996) of 0.11 to 0.31 mm/year using the MIS 5e highstand according to the U/Th dating of *T*1 near Tipaza by Stearns and Thurber (1965) and with the uplift rate estimates by Strzerzynski et al. (2010) of 0.10 ± 0.02 mm/year using the upper surface elevation of the Pliocene deposits near Algiers. They are also consistent with estimates calculated on coasts of Northern Africa and southern Spain (up to 0.2 mm/year) (e.g., Abad et al. 2013, Pedoja et al. 2013, 2014 see references therein). By contrast, the uplift rates deduced by Maouche et al. (2011) (i.e., 0.84–1.2 mm/year) is about one order of magnitude higher.

Taking into account uncertainties and a constant uplift rates extrapolated up to middle-to-upper Pleistocene, the upper rasa (*T*8) might be carved between 0.9 and 4.7 Ma (without correction for eustasy) or between 0.8 and 6.6 Ma (with correction for eustasy). However, note that this age range is only indicative since uplift rates are not necessarily constant through longer geological time (i.e., >0.5 Ma).

In the Algiers massif, the three upper rasas (*T*8, *T*9, and *T*10) overlook by a minimum of ~60 m the top of the Pliocene Gilbert-delta filling the Messinian canyon (Rubino et al. 2007). Consequently, we interpret the *T*8, *T*9, and *T*10 rasas as older than the canyon incision and filling that occurred between 5.9 and 2 Ma (Fig. 7). Furthermore, the three upper rasas are located on the Algiers massif, an allochthonous unit which collided as the other Kabylian blocks with the African plate margin during the Lower Miocene (Bouillin 1986). Consequently, the formation of the *T*8 to *T*10 rasas is certainly bracketed between the Messinian Salinity Crisis (5.9 Ma) and the lower Miocene collision (18–15 Ma) (Fig. 7). They could be associated with the three highstands recognized on the eustatic curves (Miller et al. 2005; Kominz et al. 2008), and recorded in Miocene deposits in Tunisia (Gharsalli et al. 2013), and/or producing abandonment surfaces (Clauzon et al. 1996; Champion et al. 2000; Besson et al. 2005; Rubino and Clauzon 2008; Molliex et al. 2011) during the late Tortonian (7 Ma), the Serravalien (11–12 Ma), and the Laghian (14–16 Ma), respectively (Fig. 7).

The interpolated age for *T*8 (0.8 to 6.6 Ma), calculated using the Middle-Upper Pleistocene uplift rates, is much younger than the age given by the above geological
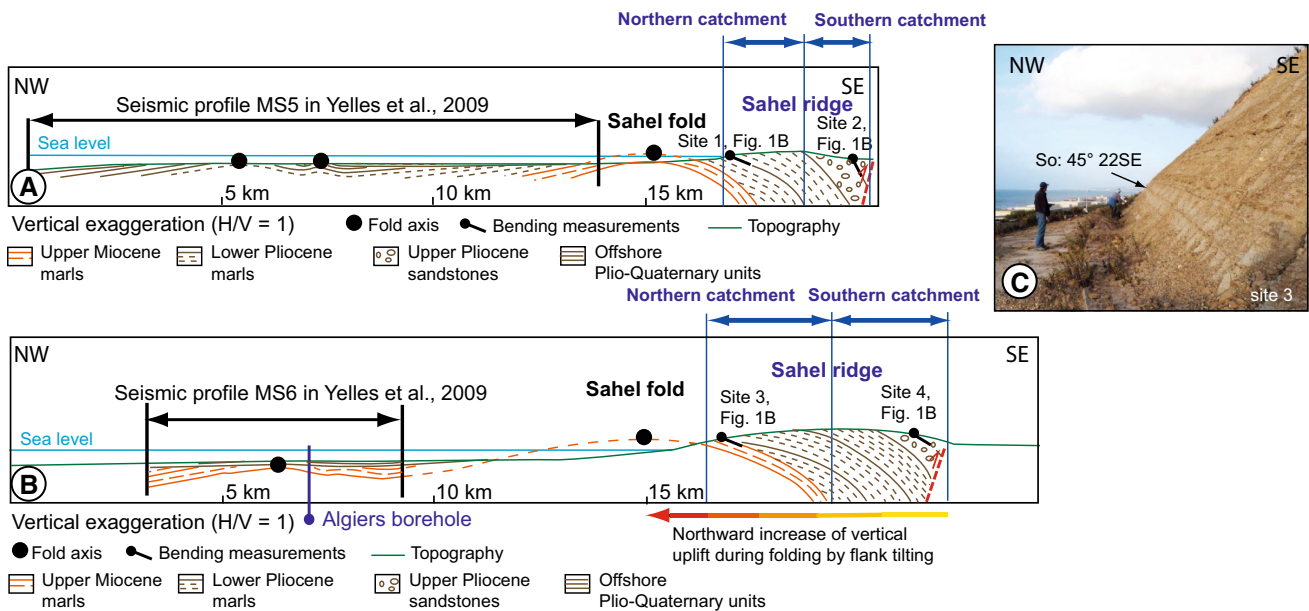
Fig. 6 Simplified cross section extending from the Sahel ridge to the offshore. **a** NW–SE geological cross section of the Sahel ridge near Tipaza and the northern offshore anticline (location on Fig. 1b) showing the possible location of the Sahel anticline axial plane (*black dot*) according to structural measurements at sites 1 and 2 (Fig. 1b), seismic profile MIS5 by Yelles et al. (2009), and the Algiers borehole (Burollet et al. 1978). **b** NW–SE geological cross section of the Sahel ridge near Mazafran valley and of the northern offshore anti-

cline (location on Fig. 1b) showing the possible location of the Sahel anticline axial plane (*black dot*) according to structural measurements at sites 3 and 4 (Fig. 1b) and seismic profile MIS6 in Yelles et al. (2009). Horizontal *yellow to red arrow* indicates the spatial variation of uplift rates along the southern limb of the Sahel anticline due to folding. **c** Picture taken at site 3 showing the Pliocene marls dipping to the south near the Mediterranean coast (see Fig. 1 for location)
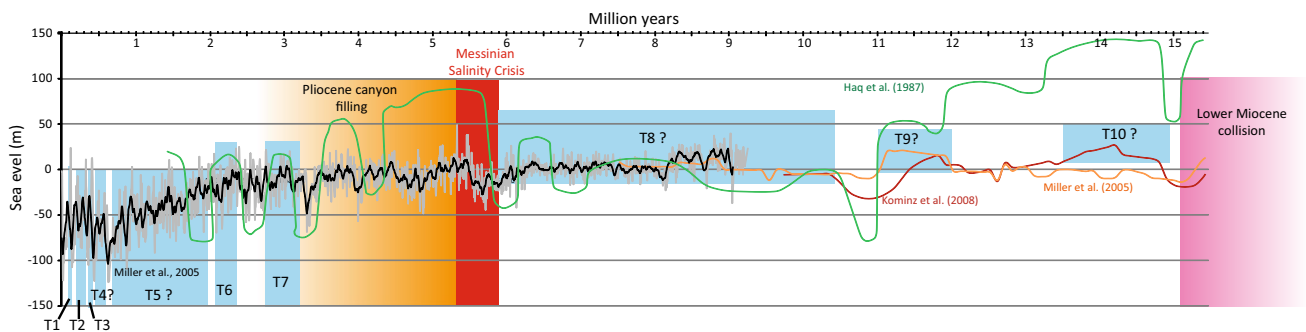
Fig. 7 Possible relationship between sea-level estimates for the past 15 Ma (Haq et al. 1987; Miller et al. 2005; Kominz et al. 2008), marine terraces/rasas, and geological events of the studied zone

correlations (~7 Ma). The discrepancy could suggest, if proved, an increase in uplift rates since the Upper Miocene. This analysis suggest the onset or the activity pulse of an offshore fold or fault near the Algiers massif inducing uplift of this massif during the Pliocene/Pleistocene.

The shoreline of rasa *T*7 is found approximately at the same elevation of the top of the Pliocene Gilbert-delta. On the topographic map visualized by the DEM image of Fig. 2a, it slightly penetrates southward the northern boundary of the upper pliocene sandstone unit (associated with

topset features), indicating that it is slightly nested within these deposits. Consequently, the caving of rasa *T*7 probably occurred after the Pliocene canyon filling beginning at 3.6 Ma (Yassini, 1975) and before the major decrease of the sea level associated with the intensification of the glacio-eustatic cycles at 2.6 Ma (Miller et al. 2005; Lisiecki and Raymo 2005) (Fig. 7).

After 2.6 Ma, the next peak in the eustatic curves (Miller et al. 2005, 2011) occurred during the Gelasian period (~2.4 Ma) and is associated with a global high

aridity period (Quade et al. 1995; Retallack 2001; Griffin 2002) (Fig. 7). The petrocalcic horizon preserved on rasa *T*6 is probably an heritage of this arid event as observed elsewhere along the Mediterranean shores (Fig. 3d) (Vogt 1984; Magaldi et al. 1989). According to the "circular" geometry of the *T*6 shoreline angle around the Algiers massif and the *T*5 "straight" shoreline angle from the Algiers massif to the Sahel ridge, the Algiers massif was once an island. During late Cenozoic, this paleo-island was "integrated" to the nearby mainland at the moment of formation of the *T*5 marine terrace (Fig. 8), a classical coastal evolution (see Fig. 8, Pedoja et al. 2014). Ages of *T*5 and *T*4 marine terraces or rasas purported older than *T*3 marine terrace (correlated to the MIS 11) must be bracketed between 2.4 Ma and 400 ka.

Morpho-tectonic interpretations and Miocene to Quaternary coastal evolution

We postulated that the climatic conditions are uniform within the studied area (~600 km2). Consequently, the cross-studies of the coastal sequences and the drainage developed on them allow us to determine how morphometric indices are sensitive to spatial variations of uplift rates and to the lithology.

It appears that the HI parameters are sensitive to the lithology: Lowest HI values (HI < 0.5) mainly correspond to the outcrop area of soft Pliocene marls (Fig. 5b). This soft lithology is rapidly eroded by the drainage system that can quickly propagate laterally. However, in most of the flanks of the Sahel ridge, almost just one lithology outcrops (Fig. 1b); therefore, the variations of the morphologic parameters on these areas are more likely reflecting the tectonic signal.

We detect rough correlations between the two geomorphic values of the northern Sahel catchments and the uplift of the *T*5 rasa (Fig. 5). Consequently, uplift gradient on zones without marine terrace shoreline angles, as the southern flank of the Sahel ridge or the southern part of the Algiers massif, could be inferred from the analysis of the values of two morphometric parameters.

The Sahel ridge has been interpreted as an anticline ending westward near Tipaza (Aymé 1952; Saoudi 1989; Maouche et al. 2011) (Fig. 1b). Folding started before the Pliocene because the upper Miocene/Pliocene discordance (higher dip of Miocene strata in comparison with Pliocene strata) observed on the cross section of the Sahel ridge along the Mazafran valley indicates that upper Miocene strata were already deformed before the Pliocene (Aymée et al. 1954). This timing of folding is also highlighted for the eastern neighboring offshore anticlines with similar discordances observed on seismic profiles (MS6 profile for Yelles et al. 2009; Figure 11 profile for Strzerzynski et al.

2010) (Figs. 1b, 6). Consequently, these two anticlines already existed during the Late Miocene. According to the interpreted age of the upper rasa *T*7 on top of the Sahel ridge (3.6–2.6 Ma), we suggest that the emergence of the Sahel ridge would began between 3.6 and 2.6 Ma (Fig. 8). Thus, this emergence is younger than the onset of the Sahel folding indicating an offshore deformation before Upper Pliocene.

We propose an offshore location for the Sahel fold axis. An axis located offshore, not far from the coastline rather than along the ridge crest, better agrees with the onshore monocline structure observed on the outcrops on the flanks of the Mazafran river valley (Aymée et al. 1954) and the two outcrops of south-dipping marls observed along the northern part of the ridge (sites 1 and 2, Figs. 1b, 7). The Sahel ridge could correspond to the southern flank of a partially emerged Sahel anticline submitted to marine erosion that has erased the topography of the northern limb (Fig. 6). The leveling of the northern flank of the Sahel anticline induces the formation of rasas and marine terraces directly on Lower Pliocene/Miocene marls forming the inside of the anticline (Fig. 3d, e). Assuming that the coastline is located near the fold axis, uplift rates deduced from the analyses of the lower marine terraces should correspond to the maximum uplift produced by the folding (Fig. 6b).

North–south variations through the Sahel ridge are observed in the morphometric parameter values, with asymmetry in Re and HI values on both sides of the Sahel crest (Fig. 5). This difference can be interpreted in various ways. (1) It should result from a difference of erodibility between the flanks of the Sahel ridge, with a softer lithology to the south than to the north. However, the erodibility of marine terraces (a few meters of cemented sandstones and pebbles) outcropping on the northern flank is probably not very different than the one of the Upper Pliocene unit (hard calcareous cemented sandstones) on the southern flank (Figs. 1b, 3d, e). (2) It can also results from the base level discrepancy between the northern and the southern Sahel catchments. The base level of the streams that drain the southern flank of the Sahel ridge is 50 m higher than the base level of the streams draining its northern flank. This difference of elevation corresponds to ~1/5 of the total relief. It could favor the achievement of an equilibrium state more rapidly than the northern rivers. However, the length of catchments is similar on both sides of the Sahel crest (Fig. 5). Thus, with a lesser local relief, the southern catchments present lower slope that induces a lower efficiency of erosion which slows the achievement of the equilibrium state. (3) It could be explained by a possible difference in age of drained landscape on both sides of the Sahel crest. The northern flank of the ridge is rejuvenated by the staircase formation of marine terraces in Pleistocene time. However, we also observed marine terraces on
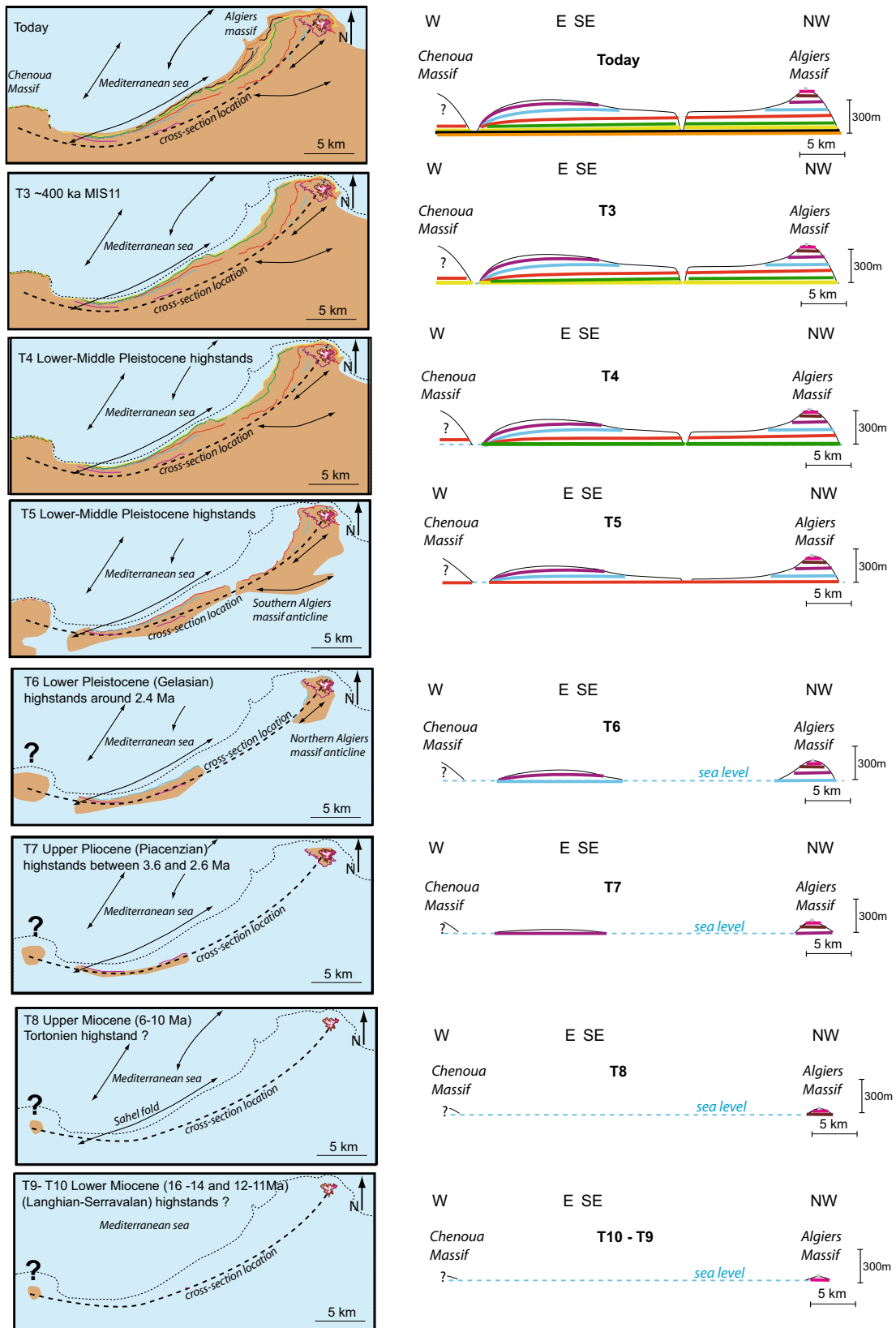
Fig. 8 Geographic and tectonic evolution of the central Algerian coast from the Miocene onward associated with the marine terrace elevation profiles. *Line with arrows* indicates the anticline axis. *Blue and brown* zones are offshore and onshore areas, respectively. *The color used* to indicate terraces and rasas are the same than on Fig. 2a

the southern flank of the Sahel ridge (Fig. 3a) what suggests that both flanks of the ridge emerged recently. (4) It also can be explained by a northward positive gradient in uplift. Indeed, high values of HI and low Re values should be explained by higher uplift rates of the northern flank of the Sahel ridge than to the south. This northward increase in uplift rates could be explained by the southward tilting of the southern fold flank induced by the folding of Sahel (Fig. 6b). This explanation is thus the one that fits better with the geomorphic and geological data.

We also interpret the westward tilting of the upper rasas and marine terraces on the western Sahel ridge termination as the consequence of folding expressed on the fold lateral terminations (Figs. 1b, 2c, 3c). Along the fold axis, the uplift of T3, T5, T7 increases from the western termination to the central part of the fold (Fig. 2c). This interpretation agrees with the quantitative geomorphic results showing an eastward increase in the HI values and the decrease in Re values from Tipaza to Bou Haroun (Fig. 5).

To the west near Tipaza, T7, T5, and 73 elevations decrease rapidly (Fig. 2c). This westward elevation decrease evidences their westward tilting; the magnitude of tilt is decreasing from the older to the younger terraces (Figs. 2c, 3c). This tilting expresses the western lateral fold termination of the Sahel anticline. Tilting rates have been estimated using the westward inclination of the T3 to T7 terraces (Fig. 2c) and interpreted terrace ages at 0.25°/Ma for T3 (~400 ka) and 0.5°/Ma for T7 (~3 Ma), suggesting a decrease in folding rate between T7 and T3 formation. The termination of the fold to the west is probably due to the presence of the Chenoua massif, which may play the role of a buttress, as it corresponds to the basement of the internal zones (Fig. 1b). This buttress is bounded to the south by a NW-dipping reverse fault whose motion may have affected the Pliocene Sahel cover (Saoudi 1989). The Mont Chenoua-Tipaza earthquake (1989) and the Tipaza earthquake in 1990 evidenced the fault activity (Meghraoui 1991; Harbi et al. 2004). However, the range of uplift rates determined with lower marine terraces on both sides of this fault (transects AT1 and AT2, Figs. 2, 4), is similar or even slightly higher for the Tipaza transect (AT2) than for the Chenoua transect (AT1). It indicates that the vertical motion components along the fault are within the margin of error of our strandline's elevation measurements or negligible since MIS 11 (~400 ka). Even if the Chenoua massif is fixed without southward motion along the Chenoua fault, it could prevent by a buttress effect the westward lateral propagation of the Sahel, but not its vertical growing.

According to the mapping of the T6 and T5 rasas on the Algiers massif, the coastal sequence widened toward the south from the period of time corresponding to the formation of rasas T6 and T5 (Fig. 8). This southward widening is also evidenced by Maouche et al. (2011) even

if our mapping is different, particularly in the number of strandlines described. The folding of the northern Algiers massif anticline followed by the folding of the southern Algiers massif anticline may explain this southward propagation of the emergence (Fig. 8). Since the formation of T5, the Sahel ridge and Algiers massif are connected. HI and Re values on the Algiers massif are globally moderate (0.58 and 0.49 averaged, respectively, for Re and HI indices) (Fig. 5). These values can be interpreted as resulting from a moderate uplift rate, lower than the one determined between Bou Haroun and Mazafran valley (Fig. 4), where HI is the highest and Re values are the lowest of the studied area.

Some variations in elevations of the coastal indicators (and consequently uplift rates) as well as variations of geomorphic indices cannot be explained only by a simple single folding. For example, the elevations (and uplift) of T7 and T5 are maximum on the northern part of the Algiers massif (Fig. 2c). The shoreline of this area is close to the Khayr al Din shelf break, bounded by reverse faults (Domzig et al. 2006; Yelles et al. 2009) (Fig. 1b), and the coastal uplift pattern is probably influenced by these offshore faults.

Conclusions

Our study of the Chenoua, Sahel, and Algiers reliefs provides a new perspective on the coastal evolution of central Algeria from the Miocene onward. In this area, we identified and mapped a sequence ten successive marine terraces and rasas. Despite our limited number of U/Th dating, their interpretation confirms the correlation of T1 (2.5–11 m) with MIS 5e (last interglacial maximum, ~120 ka) and to correlate T3 (12–73 m) with MIS 11 (~400 ka). From 120 to 400 ka, coastal uplift rates increased eastward from 0.045 ± 0.025 mm/year to 0.19 ± 0.12 mm/year (apparent) or from 0.06 ± 0.06 to 0.2 ± 0.15 mm/year (corrected for eustasy). Extrapolation of these uplift rates combined with previous regional geodynamical, geomorphological, and geological studies allowed us to propose that the upper rasas (T8, T9, and T10) present on the Algiers massif are older than the Messinian Salinity Crisis and younger than the Burdigalian collision. Thus, the age of theses rasas are ranged between 15 and 6 Ma. An intermediate rasa (T7) is probably coeval from the Pliocene abandonment surface formed between 3.6 and 2.6 Ma. These correlations and interpretations imply a slight increase in the uplift rate from the Middle Miocene and onward. The comparison of quantitative geomorphic parameters with uplift variations in space allows us to better characterize the erosional pattern of coastal reliefs as well as the regional tectonics. Re and hypsometric integral values roughly correlate with uplift

rates. Furthermore, our study highlights (1) the offshore location of the Sahel fold axis, not far from the coast, (2) an interaction between the Sahel fold and the Chenoua massif acting as a buttress, and (3) temporal variation of the uplift rates since the Upper Miocene.

References

Abad M, Rodríguez-Vidal J, Aboumaria K, Zaghloul MN, Cáceres LM, Ruiz F, Martínez-Aguirre A, Izquierdo T, Chamorro S (2013) Evidence of MIS 5 sea level highstands in Gebel Mousa coast (Strait of Gibraltar, North of Africa). Geomorphology 182:133–146

Aïté R, Gélard JP (1997) Post-collisional paleostresses in the central Maghrebides (Great Kabylia, Algeria). Bull Soc Géol Fr 168:423–436

Ambraseys N, Vogt J (1988) Material for the investigation of the seismicity of the region of Algiers. European Earthquake Engineering 3:16–29

Aymé A (1952) Le quaternaire littoral des environs d'Alger. Act Congr Panaf De Prehistoire, Session II, Alger 1952:242–246

Aymé A, Aymé JM, Magné J (1954) Etude des terrains néogènes de la cluse de Mazafran (Sahel d'Alger). Travaux des collaborateurs Bulletin n° 1. Fascicle 11:129–150

Aymé A, Aymé JM, Flandrin J, Lambert A, Bétier G (1962) 1:50000 Geological map of Tipaza. Bull. Serv. Carte geol. Algérie, n°40

Bardají T, Goy JL, Zazo C, Hillaire-Marcel C, Dabrio CJ, Cabero A, Ghaleb B, Silva PG, Lario J (2009) Geomorphology 104:22–37

Besson D, Parize O, Rubino JP, Aguilar JP, Aubry MP, Beaudoin B, Berggren WA, Clauzon G, Crumeyrolle P, Dexcoté Y, Fiet N, Laccarino S, Jiménez-Moreno G, Laporte-Galaa C, Michaux J, Von Salis K, Suc JP, Reynaud JY, Wernli R (2005) Latest Burdigalian network of fluvial valleys in southeast France (western Alps): characteristics, geographic extent, age, implications. C R Geosciences 337:1045–1054

Bintanja R, Van de Wal RSW, Oerlemans J (2005) Modelled atmospheric temperatures and sea levels over the past million years. Nature 437:125–128

Boudiaf A (1996) Etude sismotéctonique de la région d'Alger et de la Kabylie (Algérie): Utilisation des modèles numériques de terrain (MNT) et de la télédétection pour la reconnaissance des structures tectoniques actives: contribution à l'évaluation de l'aléa sismique. PhD thesis, Univ. Montpellier II, France: pp 274

Bouillin JP (1986) Le bassin maghrébin: une ancienne limite entre l'Europe et l'Afrique à l'Ouest des Alpes. Bull Soc Géol France 2(4):547–558

Bouillin JP (1992) La repartition des affleurements de la Dorsale kabyle: héritage d'une segmentation mésozoïque de la marge nord-téthysienne? C R Acad Sci Paris 315(II):1127–1132

Bracène R, Frizon de Lamotte D (2002) The origin of intraplate deformation in the Atlas system of western and central Algeria: from Jurassic rifting to Cenozoic-Quaternary inversion. Tectonophysics 357:207–226

Bull WB (1985) Correlation of flights of global marine terraces. 15th Annual Geomorphology Symposium:129–152

Burollet PF, Said A, Trouve P (1978) Slim holes drilled on the Algerian shelf. Initial Rep Deep Sea Drill Proj 42(2):1181–1184

Calais E, DeMets C, Nocquet JM (2003) Evidence for a post-3.16-Ma change in Nubia-Eurasia-North America plate motions? Earth Planet Sci Lett 216:81–91

Caputo R (2007) Sea-level curves: perplexities of an end-user in morphotectonic applications. Glob. Planet. Change 57:417–423

Carminati E, Wortel MJR, Spakman W, Sabadini R (1998) The role of slab detachment process in the opening of the western central Mediterranean basins: some geological and geophysical evidence. Earth Planet Sci Lett 160:651–665. doi:10.1016/S0012-821X(98)00118-6

Champion C, Choukroune P, Clauzon G (2000) La déformation post-Miocène en Provence occidentale. Geodin Acta 13:67–85

Chappell J (1974) Geology of Coral Terraces, Huon Peninsula, New Guinea: a study of Quaternary Tectonic Movements and Sea Level Changes. Geol Soc Am Bull 85:553–570

Cheng KY, Hung JH, Chang HC, Tsai H, Sung QC (2012) Scale independence of basin hypsometry and steady state topography. Geomorphology 171–172:1–11

Clauzon G, Rubino JL (1992) Les Gilbert-deltas pliocènes du golfe du Lion et de Ligurie: des constructions sédimentaires originales consécutives à la crise de salinité messinienne. Livret guide de l'excursion ANDRA: pp 127

Clauzon G, Suc JP, Gautier F, Berger A, Loutre MF (1996) Alternate interpretation of the Messinian salinity crisis: controversy resolved? Geology 24:363–366

Cloethingh S, Wortel R, Vlaar NJ (1989) On the initiation of subduction zones. Pageoph 129:7–25

Creveling JR, Mitrovica JX, Hay CC, Austermann J, Kopp RE (2015) Revisiting tectonics corrections applied to Pleistocene sea-level highstands. Quat Sci Rev 11:72–80

De Lamothe G (1911) Les anciennes lignes de rivage du Sahel d'Alger et d'une partie de la côte Algérienne. Mem Soc Géol France, C R 4eme série (1):288

DeMets C, Gordon R, Argus DF, Stein S (1990) Current plate motions. Geophys J Int 181:425–478

Déverchère J, Mercier de Lépinay B, Cattaneo A, Strzerzynski P, Calais, E, Domzig A, Bracène R (2010) Comment on Zemmouri earthquake rupture zone (Mw 6.8, Algeria): Aftershocks sequence relocation and 3D velocity model by Ayadi et al. J Geophys Res 115, B04320, doi:10.1029/2008JB006190

Déverchère J, Yelles K, Domzig A, Mercier de Lépinay B, Bouillin JP, Gaullier V, Bracène R, Calais E, Savoye B, Kherroubi A, Le Roy P, Pauc H, Dan G (2005) Active thrust faulting offshore Boumerdes, Algeria, and its relations to the 2003 Mw 6.9 earthquake. Geophys Res Lett 32, L04311. doi:10.1029/2004GL021646

Domzig A, Yelles K, Le Roy C, Déverchère J, Bouillin JP, Bracene R, Mercier de Lépinay B, Le Roy P, Calais E, Kherroubi A, Gaullier V, Savoye B, Pauc H (2006) Searching for the Africa-Eurasia Miocène boundary offshore western Algeria (MARADJA'03 cruise). C R Geosciences 338:80–91

Dorale JA, Onac BP, Fornós JJ, Ginés J, Ginés A, Tuccimei P, Peate DW (2010) Sea-level highstand 81,000 Years ago in Mallorca. Science 327:860–863

Duggen S, Hoernle K, Van den Bogaard P, Harris C (2004) Magmatic evolution of the Alboran region: the role of subduction in forming the western Mediterranean and causing the Messinian Salinity Crisis. Earth Planet Sci Lett 218:91–108

Durand-Delga M (1969) Mise au point sur la structure du Nord-Est de la Berberie. Bull Serv Carte Géol Algérie 39:89–131

Dutton A, Lambeck K (2012) Ice volume and sea level during the Last Interglacial. Science 337:216–219

Duvall A, Kirby E, Burbank D (2004) Tectonic and lithologic controls on bedrock channel profiles and processes in coastal California. J Geophys Res 109(F3002):1–18

Ficheur ME, Jacob M (1911) 1:50000 Geological map of Kolea. Bull. Serv. Carte geol. Algérie, n 41

Frizon de Lamotte D, Saint Bezar B, Bracene R, Mercier E (2000) The two main steps of the Atlas building and geodynamics of the western Mediterranean. Tectonics 19:740–761

Gharsalli R, Zouaghi T, Soussi M, Chebbi R, Khomsi S, Bédir M (2013) Seismic sequence stratigraphy of Miocene deposits related to eustatic, tectonic and climatic events, Cap Bon Peninsula, northeastern Tunisia. C R Geosciences 345:401–417

Gibbard P, Head MJ, Walker MJC (2010) Formal ratification of the quaternary system/period and the pleistocene series/epoch with a base at 2.58 Ma. J Quat Sci 25:96–102

Gilbert GK (1899) Ripple-Marks and Cross Bedding. Bull Geol Soc Amer 10:135–140

Glangeaud L (1932) Etude géologique de la région littorale de la province d'Alger. Bull Serv Carte géol Alger, 2eme série (8): pp 608

Glangeaud L, Aymé A, Caire A, Mattauer M, Miraour P (1952) Histoire géologique de la province d'Alger. XIXe congrès géologique international, Monographies régionales, 1ere série: Algérie 25: pp 141

Griffin DL (2002) Aridity and humidity: two aspects of the late Miocene climate of North Africa and the Mediterranean. Palaeo3 182:65–91

Guilcher A (1974) Les "rasas": un problème de morphologie littorale générale. Ann Geophys 83:1–33

Hamaï L (2011) Etude gravimétrique de la Mitidja Occidentale. Unpublished report, Univ, Houari Boumediene-Alger

Haq BU, Hardenbol J, Vail PR (1987) Chronology of fluctuating sea levels since the Triassic (250 million years ago to present). Science 235:1156–1167

Harbi A, Maouche S, Ayadi A, Benouar D, Panza GF, Benhallou H (2004) Seismicity and tectonics structures in the site of Algiers and its surroundings: a step towards microzonation. Pure appl Geophys 161:949–967

Harbi A, Maouche S, Vaccari F, Aoudia A, Oussadou F, Panza GF, Benouar D (2007) Seismicity, Seismic Input and Site effects in the Sahel-Algiers Region (North Algeria). Soil Dynamics and Earthquake Engineering 27(5):427–447

Hearty PJ, Hollin JT, Neumann AC, O'Leary MJ, McCulloch M (2007) Global sea-level fluctuations during the last interglaciation (MIS 5e). Quatern Sci Rev 26(17–18):2090–2112

Heddar A, Authemayou C, Djellit H, Yelles AK, Déverchère J, Gharbi S, Boudiaf A, Van Vliet Lanoe B (2013) Preliminary results of a paleoseismological analysis along the Sahel fault (Algeria): new evidence for historical seismic events. Quat Int 302:210–223

Hurtrez JE, Sol C, Lucazeau F (1999) Effect of drainage area on hypsometry from an analysis of small-scale drainage basins in the Siwalik Hills (central Nepal). Earth Surf Proc Land 24:799–808

James NP, Mountjoy EW, Omura A (1971) An early Wisconsin reef Terrace at Barbados, West Indies, and its climatic implications. Geol Soc Am Bull 82:2011–2018

Jolivet L, Faccenna C (2000) Mediterranean extension and Africa-Eurasia collision. Tectonics 19(6):1095–1106

King G, Vita Finzi C (1981) Active folding in the Algerian earthquake of 10 October 1980. Nature 292:22–26

Kleiven HF, Jansen E, Fronval T, Smith TM (2002) Intensification of Northern Hemisphere glaciations in the circum Atlantic region (3.5-2.4 Ma)—ice-rafted detritus evidence. Palaeogeogr Palaeoclimatol Palaeoecol 184:213–223

Kominz MA, Browning JV, Miller KG, Sugarman PJ, Misintseva S, Scotese CR (2008) Late Cretaceous to Miocene sea-level estimates from the New Jersey and Delaware coastal plain coreholes: an error analysis. Basin Res 20:211–226

Kopp RE, Simons FJ, Mitrovica JX, Maloof AC, Oppenheimer M (2009) Probabilistic assessment of sea level during the last interglacial stage. Nature 462:863–867

Lajoie KR (1986) Coastal Tectonics, in N. A. Press, ed., Active tectonic: Washington D,C, National Academic Press:95–124

Leprêtre A, Klingelhofer F, Graindorge D, Schnürle P, Beslier MO, Yelles K, Déverchère J, Bracene R (2013) Multiphased tectonic evolution of the Central Algerian margin from combined wide-angle and reflection seismic data off Tipaza. Algeria. J Geophys Res Solid Earth 118(8):3899–3916. doi:10.1002/jgrb.50318

Lisiecki LE, Raymo ME (2005) A Pliocene–Pleistocene stack of 57 globally distributed benthic delta 18O records. Paleoceanography 20:PA1003

Magaldi D, Ferrari GA, Carnicelli S (1989) Les accumulations carbonatées de type "calcrete" dans les sols et formations superficielles d'Italie méridionale. Méditerranée 68:51–59

Maouche S, Meghraoui M, Morhange C, Belabbes S, Bouhadad Y, Haddoum H (2011) Active coastal thrusting and folding, and uplift rate of the Sahel Anticline and Zemmouri earthquake area (Tell Atlas, Algeria). Tectonophysics 509(1–2):69–80

Mauffret A, Frizon de Lamotte D, Lallemant S, Gorini C, Maillard A (2004) E-W opening of the Algerian basin (West Mediterranean). Terra Nova 16:257–264

Maury RC, Fourcade S, Coulon C, El Azzouzi M, Bellon H, Coutelle A, Oubadi A, Semroud B, Megartsi M, Cotton J, Belanteur O, Louni-Hacini A, Piqué A, Capdevila R, Hernandez J, Réhault JP (2000) Post-collisional Neogene magmatism of the Mediterranean Maghreb margin: a consequence of slab break off. C R Acad Sci Paris 331:159–173

Medaouri M, Bracene R, Déverchère J, Graindorge D, Ouabaid A, Yelles-Chaouche A (2012) Structural styles and neogene petroleum system around the Yusuf-Habibas ridge (Alboran basin, Mediterranean sea). Lead Edge 31:776–785

Meghraoui M (1991) Blind reverse faulting system associated with the Mont Chenoua-Tipasa earthquake of 29 October 1989 (north-central Algeria). Terra Nova 3:84–93

Meghraoui M, Philip H, Albarede F, Cisternas A (1988) Trench investigations through the trace of the 1980 El Asnam thrust fault: evidence from paleoseismicity. Bull Seism Soc Am 78(2):979–999

Meghraoui M, Maouche S, Chemaa B, Cakir Z, Aoudia A, Harbi A, Alasset PJ, Ayadi A, Bouhadad Y, Benhamouda F (2004) Coastal uplift and thrust faulting associated with the Mw = 6. 8 Zemmouri, (Algeria) earthquake of 21, May 2003. Geophys Res.Lett 31:L19605. doi:10.1029/2004GL020466

Merritts D, Vincent KR (1989) Geomorphic response of coastal streams to low, intermediate, and high rates of uplift, Medocino triple junction region, northern California. Geol Soc Am Bull 101:1373–1388

Miller KG, Kominz MA, Browning JV, Wright JD, Mountain GS, Katz ME, Sugarman PJ, Cramer BS, Christie-Blick N, Pekar SF (2005) The Phanerozoic record of global sea-level change. Science 310:1293–1298

Miller KG, Mountain GS, Wright JD, Browning JV (2011) A 180-million-year record of sea level and ice volume variations from continental margin and deep-sea isotopic records. Oceanography 24(2):40–53. doi:10.5670/oceanog.2011.26

Mocochain L, Clauzon G, Bigot JY (2006) Réponses de l'endokarst ardéchois aux variations eustatiques générées par la crise de salinité messinienne. Bull Soc géol Fr 177:27–36

Molliex S, Bellier O, Terrier M, Lamarche J, Martelet G, Espurt N (2011) Tectonic and sedimentary inheritance on the structural framework of Provence (SE France): importance of the Salon-Cavaillon fault. Tectonophysics 501:1–16

Morel JL, Meghraoui M (1996) Goringe-Alboran-Tell tectonic zone: a transpression system along the Africa-Eurasia plate boundary. Geology 24:755–758

Murray-Wallace CV, Woodroffe CD (2014) In: Murray-Wallace CV, Woodroffe CD (eds) Quaternary sea-level changes: a global perspective. Cambridge University Press, United Kingdom

Nexer M, Authemayou C, Schildgen T, Hantoro WS, Molliex S, Delcaillau B, Pedoja K, Husson L, Regard V (2015) Evaluation of morphometric proxies for uplift on sequences of coral reef terraces: a case study from Sumba Island (Indonesia). Geomorphology 241:145–159

Nocquet JM, Calais E (2004) Geodetic measurements of crustal deformation in the western Mediterranean and Europe. Pure appl Geophys 161:661–681

Ota Y (1986) Marine terraces as reference surfaces in late Quaternary tectonics studies: examples from the Pacific Rim. Royal Society of New Zealand 24:357–375

Pedoja K, Husson L, Regard V, Cobbold PR, Ostanciaux E, Johnson ME, Kershaw S, Saillard M, Martinod J, Furgerot L, Weill P, Delcaillau B (2011) Relative sea-level fall since the last interglacial stage: are coasts uplifting worldwide? Earth Sci Rev 108:1–15

Pedoja K, Djellit H, Authemayou C, Deverchere J, Strzerzynski P, Heddar A, Nexer M, Boudiaf A (2013) Comment on: " Active coastal thrusting and folding, and uplift rate of the Sahel Anticline and Zemmouri earthquake area (Tell Atlas, Algeria). by Maouche et al. Tectonophysics 601:236–244

Pedoja K, Husson L, Johnson ME, Melnick D, Witt C, Pochat S, Nexer M, Delcaillau B, Pinegina T, Poprawski Y, Authemayou C, Elliot M, Regard V, Garestier F (2014) Coastal staircase sequences reflecting sea-level oscillations and tectonic uplift during the Quaternary and Neogene. Earth Sci Rev 108:1–15

Peucat JJ, Mahdjoub Y, Drareni A (1996) U-Pb and Rb-Sr geochronological evidence for late Hercynian tectonic and Alpine overthrusting in Kabylian metamorphic basement massifs (northeastern Algeria). Tectonophysics 258:195–213

Philip H, Meghraoui M (1983) Structural analysis and interpretation of the surface deformation of the Asnam earthquake of October 10, 1980. Tectonics 2:299–349

Pirazzoli PA, Radtke U, Hantoro WS, Jouannic C, Hoang CT, Causse C, Best MB (1993) A one million-year-long sequence of marine terraces on Sumba Island. Indonesia. Marine Geology 109(3–4):221–236

Quade J, Cater MLJ, Ojha PT, Adam J, Harrison MT (1995) Late Miocene environmental change in Nepal and the northern Indian subcontinent: stable isotopic evidence from paleosols. Geol Soc Am Bull 107:1381–1397

Raymond D (1976) Evolution sédimentaire et tectonique du Nord-Ouest de la Grande Kabylie (Algérie) au cours du cycle alpin. PhD thesis, Univ. Pierre et Marie Curie, France, pp 160

Retallack GJ (2001) Cenozoic expansion of grasslands and climatic cooling. J Geol 109:407–426

Rosenbaum G, Lister SG (2004) Neogene and Quaternary rollback evolution of the Tyrrhenian Sea, the Appenines, and the Sicilian Maghrebides. Tectonics 23:TC1013. doi:10.1029/2003TC001518

Rosenbaum G, Lister GS, Duboz C (2002) Reconstruction of the tectonic evolution of the western Mediterranean since the Oligocene. J Virtual Explor 8:107–126

Rovere A, Raymo ME, Mitrovica JX, Hearty PJ, O'Leary MJ, Inglis JD (2014) The Mid-Pliocene sea-level conundrum: glacial isostasy, eustasy and dynamic topography. Earth Planet Sci Lett 387:27–33

Rubino JL, Clauzon G (2008) Upper Miocene and Pliocene Key surfaces, stratigraphic markers used to quantify Peri-Mediterranean geodynamics. (Abstr) In: Géodynamique et paléogéographique

de l'aire méditerranéenne au Mio-Pliocène: l'inteférence eustasie/tectonique. Séance spécialisée de la Société géologique de France en l'honneur de G. Clauzon, Prix Fontannes 2007. Villeurbanne, France: 63–65, 5–6 May

Rubino JL, Clauzon G, Mezla H, Casero P (2007) Les canyons messiniens et leur remplissage Pliocène le long de la Marge Nord Africaine. Paper presented at 11e Congrès Français de Sédimentologie, Caen Univ., Caen, France, 23–25 Oct

Saoudi NE (1989) Pliocène et Pléistocène inférieur et moyen du Sahel Occidental d'Alger. Entreprise Nationale du Livre, Algiers: pp174

Schettino A, Turco E (2006) Plate kinematics of the Western Mediterranean region during the Oligocene and Early Miocene. Geophys J Int 166(3):1398–1423

Schumm SA (1956) Evolution of drainage systems and slopes in badlands at Perth Amboy, New Jersey. Geol Soc Am Bull 67(5):597–646

Serpelloni E, Vannucci G, Pondrelli S, Argnani A, Casula G, Anzidei M, Baldi P, Gasperini P (2007) Kinematics of the Western Africa-Eurasia plate boundary from focal mechanisms and GPS data. Geophys J Int 169(3):1180–1200. doi:10.1111/j.1365-246X.2007.03367.x

Siddal M, Chappell J, Potter EK (2006) Eustatic sea level during past interglacials. In: Sirocko F, Claussen M, Sanchez Goñi MF, Litt T (Eds.) The Climate of Past Interglacials. Elsevier, Amsterdam:75–92

Snyder NP, Whipple KX, Tucker GE, Merritts DJ (2000) Landscape response to tectonic forcing: digital elevation model analysis of stream profiles in the Mendocino triple junction region, northern California. Geol Soc Am Bull 112(8):1250–1263

Snyder NP, Whipple KX, Tuker GE, Merrits DJ (2003) Channel response to tectonic forcing: field analysis of stream morphology and hydrology in the Mendocino triple junction region, northern California. Geomorphology 53:97–127

Stearns CE, Thurber DL (1965) 230Th-234U dates of late Pleistocene marine fossils from the Mediterranean and Moroccan littorals. Quaternaria 7:29–42

Sten S, Cloethingh S, Sleep H (1989) Passive margin earthquakes, stresses and rheology. In: Grgersen, S and Basham PW (eds) Earthquakes at North-Atlantic Passive Margins; Neotectonics and Postglacial Rebound. NATO ASI Series, Series C: Mathematical and Physical Sciences, 266, 231–259

Stich D, Serpelloni E, Mancilla F, Morales J (2006) Kinematics of the Iberia-Maghreb plate contact from seismic moment tensors and GPS observations. Tectonophysics 426(3–4):295–317

Strahler AN (1952) Hypsometric (area-altitude) analysis of erosional topography. Geol Soc Am Bull 63:1117–1142

Strzerzynski P, Déverchère J, Cattaneo A, Domzig A, Yelles K, Mercier de Lépinay B, Babonneau N, Boudiaf A (2010) Tectonic inheritance and Pliocene-Pleistocene inversion of the Algerian margin around Algiers: insights from multibeam and seismic reflection data. Tectonics. doi:10.1029/2009TC002547

Thomas G (1976) Mise en valeur de décrochements dextres Est-Ouest d'âge quaternaire en Algérie nord occidentale. C R Acad Sci Paris, série D(283):893–896

Vogt T (1984) croutes calciares: types et genese- exemple d'Afrique du Nord et de France Mediterraneenne. PhD thesis, Univ. L. Pasteur, Strasbourg, France: pp 228

Wolin E, Stein S, Pazzaglia F, Meltzer A, Kafka A (2012) Berti C (2012) Mineral, Virginia, earthquake illustrates seismicity of a passive-aggressive margin. Geophys Res Lett 39:L02305. doi:10.1029/2011GL050310

Yassini I (1975) Planktonic foraminiferal biozonation of neogene deposits in the "Sahel" of Algier, Algeria. Rivista Italiana di Paleontologia 81:89–120

Yelles AK, Boudiaf A, Djellit H, Bracene R (2006) La tectonique active de la région Nord-algérienne. C R Geosciences 338:126–139

Yelles AK, Domzig A, Déverchère J, Bracène R, Mercier de Lépinay B, Strzerzynski P, Bertrand G, Boudiaf A, Winter T, Kherroubi A, Le Roy P, Djellit H (2009) Evidence for large active fault offshore west Algiers, Algeria, and seismotectonic implications. Tectonophysics 475:98–116